Efficient and sustained optogenetic control of sensory and cardiac systems

Alexey Alekseev[1,2,3,4,5*], Victoria Hunniford[1,3,4,5*], Maria Zerche[1,2,3,4,6*], Marcus Jeschke[1,4,7*], Fadhel El May[1,5*], Anna Vavakou[1,3,4,5*], Dominique Siegenthaler[3,4,8,9,10*], Marc A. Hüser[4,6,11**], Svenja M. Kiehn[11**], Aida Garrido-Charles[1,2,3,4**], Alexander Meyer[6], Adrian Rambousky[1,4,7,12], Theocharis Alvanos[1,5,**], Isabel Witzke[1,2], Keila Dara Rojas-Garcia[10], Martin Draband[11], Lukas Cyganek[3,13,14,15], Eric Klein[16], Patrick Ruther[16], Antoine Huet[1,3,5,17,18], Stuart Trenholm[10], Emilie Macé[3,4,8,9], Kathrin Kusch[1,4,5,12], Tobias Bruegmann[3,4,11,16], Bettina J. Wolf[1,3,4,5#], Thomas Mager[1,2,3,4#], and Tobias Moser[1,3,4,5,17#]

[1]Institute for Auditory Neuroscience and InnerEarLab, University Medical Center Göttingen, Germany
[2]Advanced Optogenes Group, Institute for Auditory Neuroscience, University Medical Center Göttingen, Germany
[3]Cluster of Excellence "Multiscale Bioimaging: from Molecular Machines to Networks of Excitable Cells" (MBExC), University of Göttingen, Germany
[4]Else Kröner Fresenius Center for Optogenetic Therapies, University Medical Center Göttingen, Germany
[5]Auditory Neuroscience and Synaptic Nanophysiology Group, Max-Planck-Institute for Multidisciplinary Sciences, Göttingen, Germany
[6]Department of Otolaryngology, University Medical Center Göttingen, Germany
[7]Cognitive Hearing in Primates Group, Auditory Neuroscience and Optogenetics laboratory, German Primate Center, Göttingen, Germany
[8]Brain-Wide Circuits for Behavior Research Group, Max Planck Institute for Biological Intelligence, Planegg, Germany
[9]Dynamics of Excitable Cell Networks Group, Department of Ophthalmology, University Medical Center Göttingen, Göttingen, Germany
[10]Montreal Neurological Institute, McGill University, Montreal, Canada
[11]Institute for Cardiovascular Physiology, University Medical Center Göttingen, Göttingen, Germany
[12]Functional Auditory Genomics Group, Auditory Neuroscience and Optogenetics laboratory, German Primate Center, Göttingen, Germany
[13]Stem Cell Unit, Clinic for Cardiology and Pneumology, University Medical Center Göttingen, Göttingen, Germany;
[14]German Center for Cardiovascular Research (DZHK), Partner site Göttingen, Göttingen, Germany
[15]Translational Neuroinflammation and Automated Microscopy, Fraunhofer Institute for Translational Medicine and Pharmacology ITMP, Göttingen, Germany.
[16]Department of Microsystems Engineering (IMTEK), University of Freiburg, 79110 Freiburg, Germany
[17]Auditory Neuroscience and Optogenetics laboratory, German Primate Center, Göttingen, Germany
[18]Auditory Circuits Lab, Institute for Auditory Neuroscience, University Medical Center Göttingen, Germany

[*]shared first, [**]shared second, [#]shared corresponding

Abstract

Optogenetic control of cells is a key life sciences method and promises novel therapies. Here we report on ChReef, an improved variant of the channelrhodopsin ChRmine. ChReef offers minimal photocurrent desensitization, a unitary conductance of 80 fS and closing kinetics of 30 ms, which together enable reliable optogenetic control of cells at low light levels (nano-Joule) with good temporal fidelity and allows sustained stimulation. We demonstrate efficient and reliable red-light pacing and depolarization block of ChReef-expressing cardiomyocyte clusters. Towards clinical application we used AAV-based gene transfer to express ChReef in retinal ganglion cells where it restores visual function in blind mice with light sources as weak as an iPad screen. Toward optogenetic hearing restoration, ChReef enables stimulation of the auditory pathway in rodents and non-human primates with nano-Joule threshold enabling efficient and frequency-specific stimulation by LED-based optical cochlear implants. Thus, ChReef bears great potential for life sciences and clinical application.

Keywords: channelrhodopsin, automated patch-clamp, neural circuit, hearing, visual system, cardiomyocyte

Running title:

Efficient optogenetic control of sensory pathways and cardiomyocytes

53 With an ever-growing toolkit of light-sensitive proteins (opsins) and optical devices, optogenetics
54 has driven progress in the life sciences[1]. It is routinely used to manipulate the activity of specific
55 cell types *in vivo* in genetically tractable species such as mice, fish, or flies. In medicine, concurring
56 progress in optogenetic modification of retinal neurons and visual coding by light amplifying
57 goggles has enabled a first successful clinical application of optogenetics for vision restoration[2].
58 Yet, several challenges remain to be tackled for realizing the full potential of optogenetics. For
59 example, the low single-channel conductance of non-selective cation conducting
60 channelrhodopsins (ChRs: e.g. 40 fS for ChR2[3]) limits their utility. The required high levels of
61 expression and high light doses bear the risk of proteostatic stress and phototoxicity in the target
62 tissue[4]. In the visual system, low single-channel conductance impedes versatile optogenetic
63 stimulation by natural light or computer screens and necessitates the use of light amplifying
64 goggles for optogenetic vision restoration. The energy demand of state-of-the-art optogenetic
65 control also challenges the power budget of medical devices such as future optical cochlear
66 implants for improved hearing restoration[4,5]. Kalium- and Anion-selective cryptophyte
67 channelrhodopsins (KCRs and ACRs) with larger single channel conductance have recently been
68 reported serving efficient inhibition of excitable cells[6,7]. Aiming for a depolarizing ChR for efficient
69 excitation, we targeted the cryptophyte ChR ChRmine that mediates large depolarizing
70 photocurrents and has red-shifted light absorption (λ_{max} = 520 nm)[8–10]. This way ChRmine, has
71 enabled control of cardiac activity of mice by light applied from outside[11] as well as implant-free
72 deep brain optogenetics[12]. Here, we demonstrate that ChRmine exhibits a comparatively high
73 unitary conductance. Yet, strong desensitization of ChRmine remains an unsolved key problem,
74 impeding applications that require sustained or high rate optogenetic stimulation. We

75 deciphered the mechanistic underpinnings of ChRmine desensitization and overcome it in the
76 ChRmine T218L/S220A variant ChReef ("**ChR** that **e**xcites **ef**ficiently") that provides advanced
77 utility when applied to cardiomyocytes (CMs) of the heart, the eye, and the ear.

78

79 **Results**

80 **ChRmine is a high unitary conductance ChR that exhibits strong light-dependent inactivation**
81 Using patch-clamp recordings from neuroblastoma-glioma cells (NG cells) expressing the
82 cryptophyte ChR ChRmine fused to TS-EYFP-ES for improved plasma membrane targeting[8,13,14],
83 we found that the stationary photocurrent of ChRmine is only about 20% of the peak current
84 (Stationary-Peak-Ratio: 0.22 ± 0.12 (n = 57), Fig. 1b, Figs. S1 and S2, Table S1). In fact, the ChRmine
85 stationary photocurrent density at saturating light intensity (Fig. 1c, J_{-60mV} = 21.6 ± 15.8 pA/pF, n
86 = 44) did not exceed that of other state of the art depolarizing ChRs (Fig. 1c, Table S2).
87 Interestingly, the stationary photocurrent showed an initial increase with light intensity followed
88 by a decrease to a submaximal value despite increasing light intensity (Fig. 1f), suggesting a
89 substrate (photon) inhibition of the partial type[15] that had, to our knowledge, not yet been
90 described previously.

91 As the unitary conductance of ChRs is too small to be directly determined by single
92 channel recordings, we investigated the variance in photocurrent ensembles using stationary and
93 non-stationary noise analysis[16]. As ChR conductance approaches the detection limit in stationary
94 noise analysis[3,6,7,17], we upscaled data collection by automated patch-clamp (Syncropatch 384,
95 Nanion) operated in synchrony with LED-based illumination (Fig. S3). This way, we could

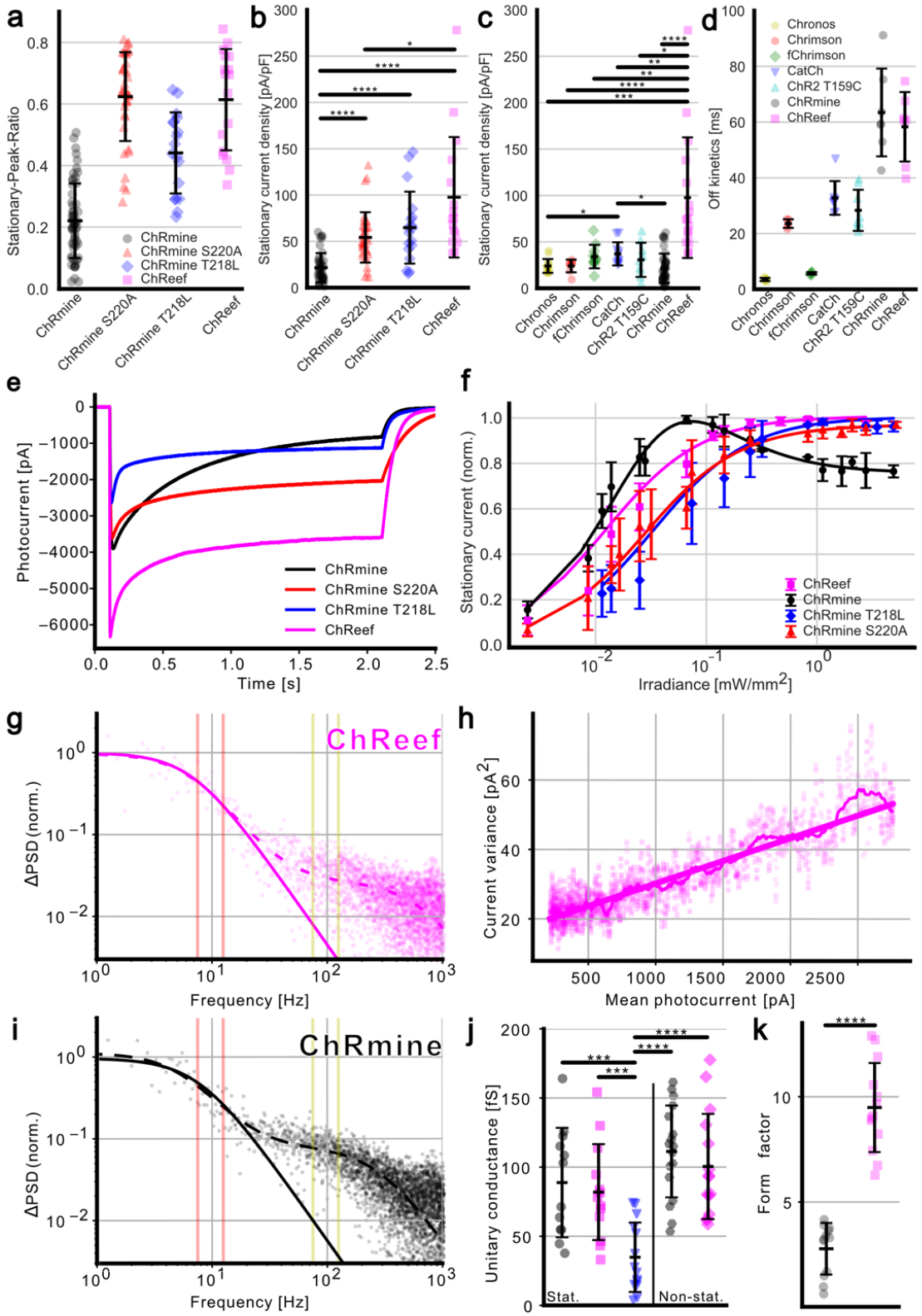
a
Stationary-Peak-Ratio
ChRmine
ChRmine S220A
ChRmine T218L
ChReef
b
Stationary current density [pA/pF]
c
Chronos
Chrimson
fChrimson
CatCh
ChR2 T159C
d
Off kinetics [ms]
e
Photocurrent [pA]
Time [s]
f
Stationary current (norm.)
Irradiance [mW/mm2]
g
ΔPSD (norm.)
Frequency [Hz]
h
Current variance [pA2]
Mean photocurrent [pA]
i
j
Unitary conductance [fS]
Stat.
Non-stat.
k
Form factor

96

Figure 1. Electrophysiological characterization of ChRmine variants. a-e, Photocurrents of NG cells expressing channelrhodopsin variants were elicited at saturating light intensity (λ = 532 nm) and recorded by whole-cell patch-clamp at a membrane potential of -60 mV. **a**, Stationary-Peak-Ratios of the photocurrents of ChRmine-TS-EYFP-ES ("ChRmine", black circle, n=57), ChRmine-TS-EYFP-ES S220A ("ChRmine S220A", red triangle, n=38), ChRmine-TS-EYFP-ES T218L ("ChRmine T218L", blue rhombus, n=18) and ChRmine-TS-EYFP-ES T218L/S220A ("ChReef", magenta square, n=21). **b**, Current densities of ChRmine variants: stationary photocurrent densities of ChRmine (n=44), ChRmine S220A (n=35), ChRmine T218L (n=18) and ChReef (n=16) at saturating light intensity. (λ = 532 nm) **c**, Stationary photocurrent densities of Chronos-EYFP (yellow pentagon, λ = 473 nm, n=14), Chrimson-EYFP (red hexagon, λ = 594 nm, n=8, f-Chrimson-EYFP (green rhombus, λ = 594 nm, n=11, [18]), CatCh-EYFP (blue triangle, λ = 473 nm, n=11) and ChR2-EYFP T159C (cyan triangle, λ = 473 nm, n=9) at saturating light intensities, ChRmine and ChReef replotted for comparison. **d**, Channel closing kinetics of ChR variants. τ_{off} values of Chronos-EYFP (pentagon, λ = 473 nm, n=8), Chrimson-EYFP (λ = 594 nm, n=5 [from ref. [18]]), f-Chrimson-EYFP (λ = 594 nm, n=5, [from ref. [18]]), CatCh-EYFP (λ = 473 nm, n=9) and ChR2-EYFP T159C (λ = 473 nm, n=8), ChRmine (λ = 532 nm, n=7) and ChReef (λ = 532 nm, n=7). **e**, Exemplary photocurrent traces of ChRmine, ChRmine S220A, ChRmine T218L and ChReef. **f**, Light intensity dependence of the normalized stationary photocurrents of ChRmine (n=7), ChRmine S220A (n=4), ChRmine T218L (n=4) and ChReef (n=4) (λ = 532 nm). The solid lines colored in red, blue, and magenta show fits to the data using a hyperbolic function. The black solid line shows a fit to the data using an equation describing a substrate inhibition of the partial type (see online methods). **g-k**, Noise analysis of ChRmine and ChReef photocurrents. **g, i**, Exemplary plots showing the difference of the power spectral densities (PSD) of whole-cell currents recorded from HEK293T cells expressing ChReef **(g)** or ChRmine **(i)** under light and dark conditions at a membrane potential of -100 mV. The PSD difference was normalized to the fitted value at 0 Hz. Solid lines: fit to the PSD difference by a single Lorentzian function, dashed line: fit by a double Lorentzian function. **h**, Non-stationary noise analysis of whole-cell photocurrents recorded at a membrane potential of -100 mV: relation between the variance of an exemplary ChReef photocurrent and its average value. Thin line: moving average of the variance, bold line: linear fit to the data. **j**, Statistical comparison of single channel conductance values of ChRmine, ChReef and CatCh obtained by stationary (grey circles for ChRmine, magenta squares for ChReef and blue triangles for CatCh) and non-stationary (grey hexagons for ChRmine and magenta diamonds for ChReef) noise analyses. **k**, Statistical comparison of PSD form factor values for ChRmine (grey circles) and ChReef (magenta squares). The form factor is defined as the ratio of mean ΔPSD values at 7.5 to 12.5 Hz (region between the red lines depicted in panels a and c) and 75 to 125 Hz (region between the yellow lines depicted in panels f and g). (p-value < 0.05 (*), 0.005 (**), 0.001 (***), 0.0001(****), the comparisons were done using Tukey´s HSD (honestly significant difference test). **a-j**, The symbols in **(b)** and horizontal bars in **(a-d, j, k)** indicate average values, the error bars show SD **(a-d, f, j, k).**

136 simultaneously record ensembles of photocurrents from dozens of HEK293 cells (holding
137 potential: −100 mV) elicited by blue light for the efficient ChR2 mutant CatCh[17] or green light for
138 ChRmine (Fig. S3).

139 Strict quality measures, regarding background noise ($I_{RMS,\ dark}$ < 5.5 pA) and stationary
140 photocurrent size (> 200 pA), limited the number of suitable recordings to 14/149 for CatCh and
141 12/71 for ChRmine. Still, a sample size sufficing statistical comparison could be obtained within
142 days, due to the highly parallelized approach. Fitting the power spectra with Lorentzian functions
143 revealed a significantly larger single channel conductance of ChRmine compared to CatCh (Fig.
144 1i, j, ChRmine: 88.8 ± 39.6 fS, n=12 vs. CatCh: 34.8 ± 25.1 fS, n=14, $p < 0.001$). We confirmed this
145 finding by non-stationary noise analysis (Fig. 1g, Fig. S4, 111.3 ± 33.2 fS (n=17); holding potential:
146 −100 mV) using short (5 ms) light pulses at a rate of 0.2 Hz to avoid desensitization. The stationary
147 noise analysis provided further insight into ChRmine function: in addition to the power spectral
148 density in the low frequency range (2.5 to 25 Hz) it also exhibited a pronounced shoulder at
149 higher frequencies (75 to 125 Hz – yellow lines, Fig. 1i). This likely indicates the presence of a
150 second, short-lived open state. We hypothesize that this state results from absorption of a
151 second photon, inducing a parallel low conducting photocycle that underlies the observed
152 substrate inhibition. Parallel photocycles have been implicated in desensitization of green algal
153 ChRs[19,20].

154

155 **Minimization of light-dependent inactivation results in exceptionally high stationary**
156 **photocurrents**

157

158 With the objective of optimizing ChRmine for life sciences and medical applications, we
159 investigated the effect of mutations at the homologous position (F219Y) and the adjacent
160 positions (T218L and S220A) to the F219Y mutation in helix 6 of ChR2, which significantly
161 accelerated channel closing in green algal ChRs[18]. The electrophysiological characterization of the
162 ChRmine mutants was carried out by manual and automated patch-clamp experiments in NG-
163 and HEK293 cells, respectively. ChRmine F219Y showed strongly reduced photocurrents and
164 channel closing kinetics (ChRmine F219Y: $\tau_{off\ (-60\ mV)}$ = 58.1 ± 5.4 ms, n=19) similar to ChRmine wt
165 (ChRmine wt: $\tau_{off\ (-60\ mV)}$ = 63.5 ± 15.7 ms, n=7) (Fig. S5, Fig. S6). We also also found similar τ_{off}
166 values for ChRmine T218L ($\tau_{off\ (-60\ mV)}$ = 59.1 ± 21.3 ms, n=7) and ChRmine T218L/S220A ("ChReef")
167 ($\tau_{off\ (-60\ mV)}$ = 58.3 ± 12.5 ms, n=7, $\tau_{off\ (-60\ mV)}$ at 36 °C: 35 ± 3 ms, n=6) (Table S1, Fig. S5, Fig. S6),
168 whereas ChRmine S220A had slower channel closing kinetics ($\tau_{off\ (-60\ mV)}$ = 152.7 ± 19.8 ms, n=6).
169 Importantly, ChRmine T218L, ChRmine S220A and ChReef showed a regular light
170 dependence (hyperbolic, sigmoidal on log-scale, Fig. 1f). Hence, the helix 6 mutants lacked the
171 light-dependent inactivation process found in wild-type ChRmine. In line with this notion,
172 photocurrent desensitization was strongly reduced in the mutants (Fig. 1a, S Fig. S1,
173 Supplementary Table 1): from ChRmine T218L (Stationary-Peak-Ratio: 0.44 ± 0.13, n=18), to
174 ChRmine S220A (Stationary-Peak-Ratio: 0.62 ± 0.14, n=38) and ChReef (Stationary-Peak-Ratio:
175 0.62 ± 0.15, n=21). ChReef showed the largest stationary photocurrent density, considerably
176 exceeding most of current state of the art ChRs (Fig. 1c, d, Supplementary Table 1 and 2) (ChReef:
177 97.6 ± 65.0 pA/pF, n=16 vs. ChRmine WT (21.6 ± 15.8 pA/pF, n=44), except for the blue light
178 activated and slowly deactivating ($\tau_{off\ (-60\ mV)}$ = 279 ± 86 ms, n=31) green algal ChR *Co*ChR
179 H94E/L112C/K264T (CoChR-3M)[21] (Fig. S5). We consider ChReef better suited for future

180 optogenetic therapies than *Co*ChR-3M, because of its more red-shifted action spectrum and its
181 much faster channel closing kinetics. These properties reduce the risk of phototoxic effects and
182 enables photostimulation at higher frequencies (Fig. 1d, Fig. S5, Fig. S7). Ion permeability ratio
183 determinations from the shift of the reversal potential upon ion replacement using the Goldman–
184 Hodgkin–Katz equation showed that the ion permeability ratios were not significantly different
185 in ChReef and ChRmine wt (Fig. S8). ChReef is an unselective cation channel (P_K/P_{Na} ~ 1) that
186 exhibits a considerable proton conductance (P_H/P_{Na} ~ 10^5) and virtually no calcium conductance.
187 In comparison, ChR2 has muhigher proton and calcium permeability (e.g. ChR2 variant CatCh[17]:
188 P_H/P_{Na} ~ 10^6, P_{Ca}/P_{Na} ~ 0.15, [17]). Hence, ChReef provides lower risk for possible adverse effects
189 resulting from Ca^{2+} and H^+ influx, which may arise upon long-term optogenetic stimulation.
190 Next, we determined the single channel conductance of ChReef which is statistically
191 indistinguishable to ChRmine (Fig. 1j; 81.9 ± 34.7 fS, n=13, stationary noise analysis and 100.5 ±
192 38.0 fS, n=15, non-stationary noise analysis). The high-frequency power spectral density
193 component found in ChRmine was not detectable for ChReef (Fig 1g, l, k), which we propose to
194 reflect a considerably accelerated transition of the parallel photocycle open state into the main
195 photocycle that results in the minimization of the light-dependent inactivation (Fig. 1 f). The
196 finding that the channel closing kinetics of ChRmine and ChReef could be fitted to a mono-
197 exponential function indicates that the short-lived second open state does not noticeably
198 contribute to the stationary photocurrent of ChRmine, in line with the suggested role of a parallel
199 photocycle in photocurrent reduction. The photocurrent desensitization kinetics of the ChRmine
200 variants at saturating light intensities could be approximated by a bi-exponential function (τ_{DES1}
201 ~ τ_{off}, τ_{DES2} > 1 s, Fig. S9). The relative amplitude of the slowly desensitizing component was much

202 smaller in ChReef than in ChRmine wt (Fig. S9), indicating the contribution of a slow process,
203 likely substrate inhibition of the partial type, to photocurrent desensitization in ChRmine wt.
204 Photocurrent desensitization generally results from the difference in the distribution of open and
205 closed states before (peak current at high intensities) and at steady-state (stationary current).
206 Experiments at suboptimal wavelength (λ ~ 632 nm) and subsaturating intensities (~ 1 mW/mm^2)
207 showed that even without sizable peak current the stationary photocurrent of ChReef remained
208 elevated (Figs. S10 and S11). The combination of high unitary conductance and minimal light-
209 dependent inactivation qualifies ChReef for efficient and sustained optogenetic stimulation.
210

211 **Optogenetic stimulation of cardiac tissue**

212 To assess the utility of ChReef for life science applications and future optogenetic therapies, we
213 turned to the cardiac, visual, and auditory systems. We first benchmarked ChReef to ChRmine
214 for pacing cardiomyocyte (CM) clusters generated from neonatal mouse hearts and upon near
215 complete AAV2/9 mediated-ChR expression (Figure 2a,b; 96 ± 1,8% for ChReef and 98 ± 0,5% for
216 ChRmine, N=2 isolations and n=5 coverslips each, unpaired student t-test, p = 0.11). We achieved
217 reliable optical pacing at 1 Hz with green (510 nm, 5 ms) and red (630 nm, 50 ms) light pulses at
218 irradiances below 100 µW/mm^2 and 350 µW/mm^2, respectively in both ChReef- and ChRmine-
219 CMs (Fig. S12a-c). Higher pacing rates increased the light requirement, in particular for red light
220 for which we found significantly lower pacing thresholds with ChReef at rates of ≥3 Hz (Fig. S12d-
221 f), likely reflecting the higher steady-state currents mediated by ChReef (Fig. S10 and S11).

222 Optogenetic cardiac defibrillation of ventricular arrhythmia[22–24] and cardioversion of
223 atrial arrhythmia[23,25,26] are exciting targets for future clinical translational[27]. Here, we compared

224 the efficiency of ChReef and ChRmine for inducing a depolarization block of CMs, considered the
225 most effective mechanism for optogenetic termination of cardiac arrhythmia[28]. Continuous
226 illumination with green light prevented electrically-evoked contraction of CM clusters with
227 significantly lower light requirements for ChReef than for ChRmine, while no effect was found in
228 non-transduced control CM clusters (Fig. 2c, d). Using red light revealed an even stronger
229 advantage of ChReef for depolarization block of CMs: contraction was prevented in 14 of 15
230 ChReef-expressing clusters compared to only 7 of 17 ChRmine-expressing clusters (Fig. 2e, f).

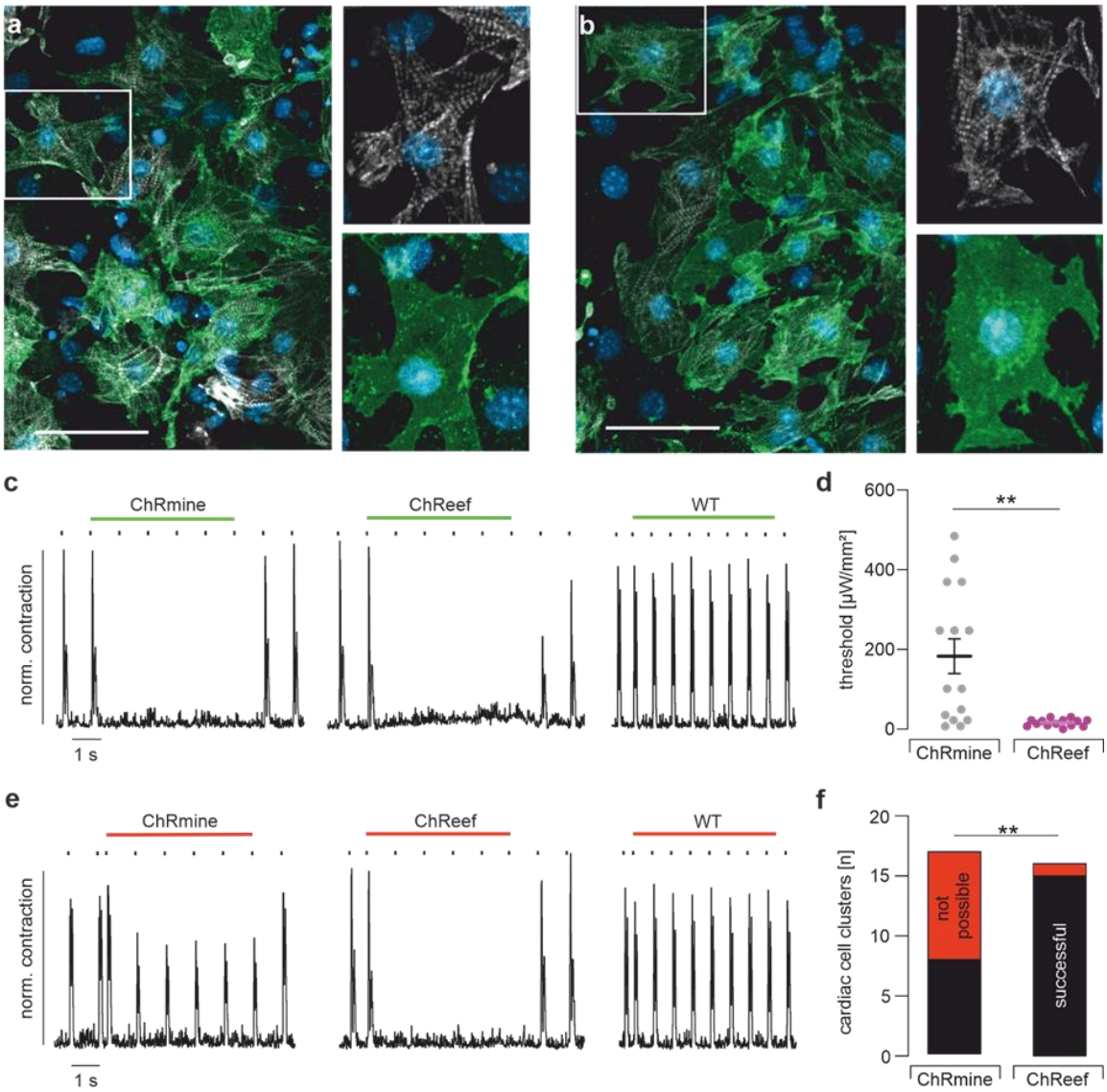

231

232 **Figure 2. Optical prevention of electrical excitation of cardiac cell clusters. a-b**, Image of a
233 cardiac cell cluster comprising neonatal mouse cardiomyocytes identified by cardiac troponin I
234 staining (white) expressing ChRmine (green) with nuclei stained by Hoechst in blue, bar equals
235 50 µm. **b**, Image of a cardiac cell cluster comprising neonatal mouse cardiomyocytes identified
236 by cardiac troponin I staining (white) expressing ChReef (green) with nuclei stained by Hoechst
237 in blue, bar equals 50 µm. **c**, Representative traces of contractions of cardiac cell clusters
238 expressing ChRmine (left) and ChReef (middle) or wild type controls (right, representative
239 example for 4 cardiac cell clusters) induced by electrical stimulation (black dots: 0.2 ms biphasic,
240 45 V) and prevented by continuous illumination with green light (green bar: 510 nm, 5 s, 36
241 $\mu W/mm^2$ for ChRmine and 14 $\mu W/mm^2$ for ChReef and 1 mW/mm^2 for WT). Note the still existing
242 contractions during the illumination in the WT example defined as unsuccessful termination. **d**,
243 Aggregated data of the required light intensities to inhibit electrical excitation with green light
244 for ChRmine (black) and ChReef (red) expressing cardiac cell clusters. Statistical comparison with
245 a two-sided unpaired student's t test ($p = 0.001$, $N = 3$ individual isolations and AAV transductions;
246 $n = 15$ for ChRmine expressing cardiac cell clusters and 14 for ChReef). **e**, Representative traces
247 of contractions of cardiac cell clusters expressing ChRmine (left) and ChReef (middle) and one
248 wild type cardiac cell cluster (right) induced by electrical stimulation (black dots: 0.2 ms biphasic,
249 45 V) and the effect of continuous illumination with red light (red bar: 630 nm, 5 s, 1 mW/mm^2
250 for ChRmine and 100 $\mu W/mm^2$ for ChReef and 1 mW/mm^2 for WT). Note the still existing
251 contractions during the illumination in the ChRmine example defined as unsuccessful
252 termination. **f**, Aggregated data of the efficiency in preventing contractions with red light
253 (maximal light intensity: 1 mW/mm^2) for ChRmine and ChReef expressing cardiac cell clusters.
254 Statistical analysis was performed with Fisher´s exact contingency test ($p = 0.0028$; $N = 3$
255 individual isolations and AAV transductions; $n = 17$ individual cardiac cell clusters for ChRmine
256 and 15 for ChReef).

257 In line with the results from neonatal mouse CMs, we found similar effects in human induced
258 pluripotent stem cell (hIPSC) derived CMs in which the increase in required light intensities with
259 higher pacing frequencies was also significantly more pronounced for ChRmine compared to
260 ChReef (Fig S13a-d). The depolarization block was only achievable in 6 out of 19 CM clusters
261 expressing ChRmine, but in all ChReef-expressing CM clusters using red light (Fig S13e). This
262 seems highly relevant, as sustained depolarization of the heart muscle upon long wavelength
263 light would be required for future transmural optogenetic termination of arrhythmia[29].

264

265

266 **Optogenetic vision restoration**

267 Optogenetic restoration of vision is currently being evaluated in clinical trials. In the PIONEER
268 trial, intravitreal injection of AAVs is used to express ChrimsonR in retinal ganglion cells (RGCs)[2]. A
269 current disadvantage of this approach is that the low light sensitivity requires light-
270 amplifying goggles that employ relatively high light intensities. This limits the dynamic range of
271 optogenetic encoding of visual information and poses a potential risk of phototoxicity for long-
272 term use. Here, we tested the potential of expressing ChReef and ChRmine in retinal ganglion
273 cells for low light optogenetic vision restoration in the rd1 mouse model of retinopathy[30]. AAV-
274 PHP.eB carrying either of the EYFP-tagged ChRs under the control of the human synapsin (hsyn)
275 promotor were intravitreally injected (Fig. 3a). Despite the use of the general neuronal hsyn
276 promoter, opsin expression was largely limited to the RGC and inner plexiform layers of the retina
277 (Fig. S14). Opsin expression in coronal brain slices was evident for RGC axons in the lateral
278 geniculate nucleus and superior colliculus (Fig. S15). Responses to optogenetic stimulation of the
279 eye to a green LED or an iPad screen positioned close to the mouse eye were recorded by
280 multielectrode arrays inserted into the contralateral primary visual cortex (V1) 3-4 weeks after
281 AAV-administration (Fig. 3b). Single-unit V1 activity could be elicited by full field LED flashes of
282 200 ms duration at 1 Hz in both ChReef and ChRmine-injected mice (Fig. 3c-f, Fig. S16).

283 For both ChReef and ChRmine, we observed cells that responded at light intensities as
284 low as 0.25 µW/mm^2 (50 nJ/mm^2, Fig. 3d arrows and Fig. S16a), which is around the light
285 intensities observed in indoor settings[31] demonstrating high light sensitivity conferred to retinal
286 ganglion cells by both ChRs. Importantly, ChReef injected animals showed stronger and more
287 sustained V1 activity compared to ChRmine, especially at low light intensities (Fig. 3c-f, Fig. S16).

288 In further support of high sensitivity vision restoration, full-field stimuli presented to the eye from
289 an iPad screen also elicited V1 activity in both ChRmine and ChReef injected mice (Fig. 3g-i).
290 Again, V1 activity was stronger and more sustained in ChReef compared to ChRmine expressing
291 animals (Fig. 3i). This indicates that ChReef enables the use of computer screens for versatile
292 visual stimulation in vision research and for restoring vision in blind patients at lower light
293 intensities.

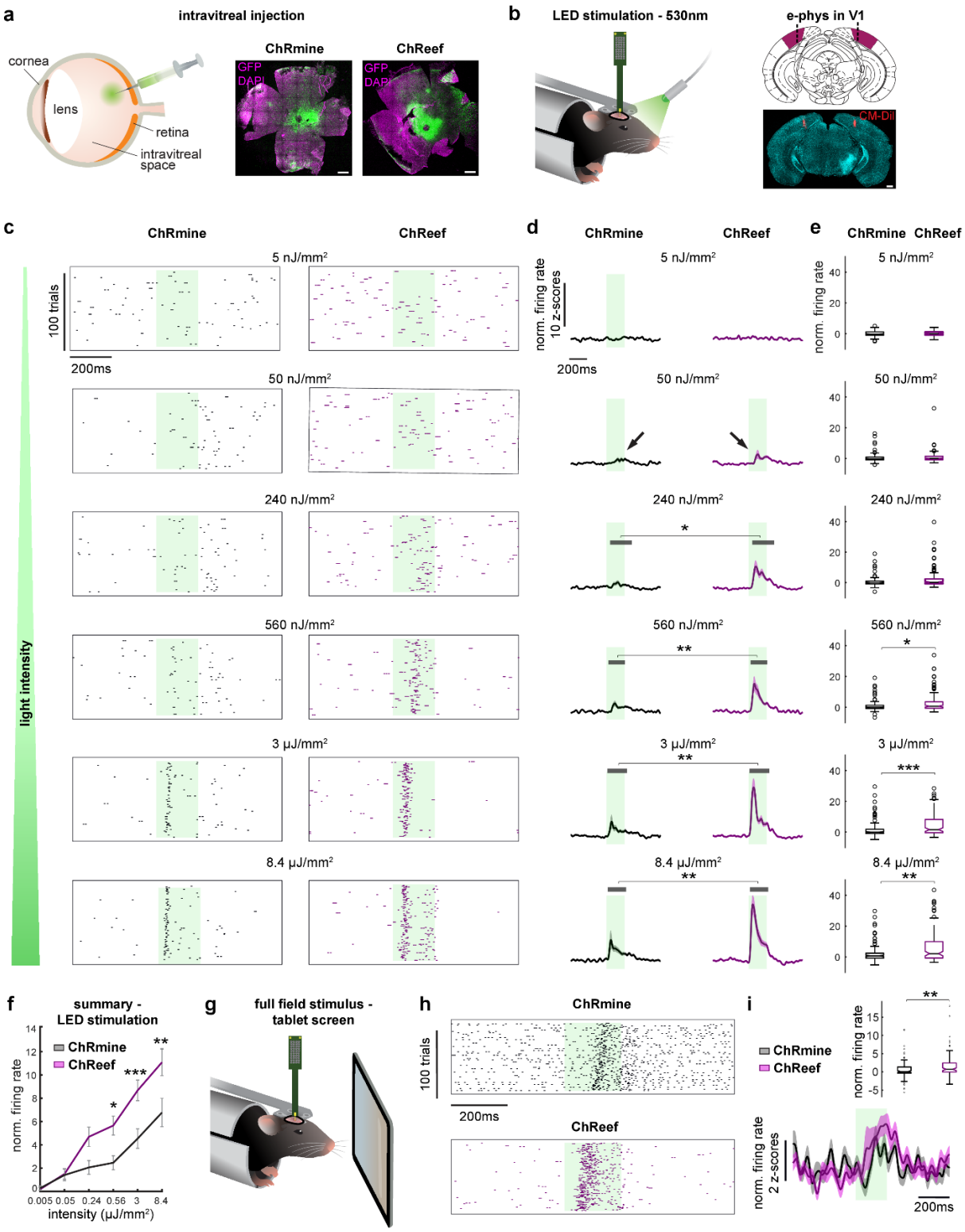

Figure 3. ChReef-mediated vision restoration in rd1 mice has low light requirements

a, Schematic representation of the intravitreal injection approach (left) and expression pattern of both opsins - ChRmine and ChReef – in retinas of rd1 mice after intravitreal injection (right). Scale bar represents 0.5mm. **b**, Vision-restored mice were presented with 200 ms flashes of green

light (530 nm) while recording extracellularly in primary visual cortex using 32-channel silicon probes (left). An example brain slice showing the probe's insertion site in V1 (right, electrode track marked by CellTracker™ CM-DiI). Scale bar represents 0.5mm. **c**, Raster plots of two example single units recorded in V1 of ChRmine- and ChReef-injected mice. **d**, Normalized average firing rates of V1 single units in response to varying light intensities. Line and shaded area represent mean ± SEM. Gray lines indicate time clusters of significant difference between the two conditions (Permutation test: see Methods, p (from top to bottom, Bonferroni-Holm corrected) = 0.4062, 0.5021, 0.0162, 0.0042, 0.0048, 0.0066), n = 151 cells in 6 mice (ChRmine), 123 cells in 6 mice (ChReef)). **e**, Average normalized firing rate during the stimulus window for the same neurons as in d (Mann-Whitney-U-test, p (from top to bottom, Bonferroni-Holm corrected) = 0.2349, 0.1468, 0.0671, 0.0451, 0.0001, 0.0049). Central line indicates median, box includes data from 25th to 75th percentile and the whiskers span the most extreme data points not considering outliers (empty circles). **f** Average normalized firing rate during the stimulus window as in **e**. Error bars represent ± SEM. **g**, Schematic depicts the experimental approach for **h-i**. In contrast to green LED flashes, here we employed an iPad screen to present white, full-field flashes of 200 ms. **h**, Raster plots of two example V1 neurons are shown. **i**, Normalized firing rates of V1 single units in response to the iPad-delivered full-field flash, n = 90 cells in 5 mice (ChRmine), 110 cells in 6 mice (ChReef). Line and shaded area represent mean ± SEM. Inset shows the average normalized firing rate during the stimulus for the same cells (Mann-Whitney-U-test, p = 0.0093).

To test if ChReef expression in the retina of rd1 mice enables behavioral responses to light, we performed the light-room/dark-room test (Fig. S17a). This tests an innate behavior of sighted mice to spend more time in the dark-room [32,33]. First, we used epifluorescence imaging to confirm robust YFP expression in the retina of intravitreally AAV-PHP.eB-hSyn-ChReef injected rd1 mice (Fig. S17b). Next, we placed injected rd1 mice as well as wildtype control (WT) and untreated rd1 mice in the light-room/dark-room environment. To control for a potential room bias, the experiment was repeated four times while alternating which room was lighted. As previously established[32], we found that sighted WT mice spent the majority of their time in the dark-room, whereas rd1 mice did not show a preference between the two rooms (Fig. S17c). Notably, all rd1 mice were outside three standard deviations (SDs) of the WT distribution. We thus used 3 SDs of the wildtype distribution as a threshold for defining if a mouse was sighted or blind. We found

331 that rd1-ChReef mice were below this threshold, and thus, similar to sighted mice (Fig. S17c),
332 preferred the dark-room revealing partial restoration of vision.

333

334 **Optogenetic stimulation of the auditory pathway**

335 Optogenetics promises to improve the restoration of hearing by cochlear implants (CIs)[4,5].
336 Electrical CIs (eCIs) used in currently ~1 M otherwise deaf users, bypass dysfunctional or lost
337 sensory hair cells by direct electrical stimulation of spiral ganglion neurons (SGNs). eCIs typically
338 enable 1-to-1 conversation in a quiet environment, yet, understanding speech in background
339 noise remains a major unmet clinical need[34]. Optogenetic SGN stimulation could transform CI
340 hearing as light, different from current, can be confined in space. Hence, optical CI (oCI) provide
341 near natural spectral selectivity of optogenetic SGN stimulation, outperforming the eCI[35,36]. One
342 of the challenges for clinical translation of the optical CI (oCI) is the increased power budget that
343 results from upscaling the number of stimulation channels (oCI: 64 planned vs. eCI: 12-24) and
344 the higher energy required per stimulus[4,5]. Using the ChRs currently available, pulse energy
345 thresholds for optogenetic SGN stimulation range from 1.500 nJ to 12.000 nJ[5] compared to 50 nJ
346 for eCI[37]. Reducing the required pulse energy by greater light efficiency of optogenetic SGN
347 stimulation remains a key objective *en route* to clinical translation of the oCI. Here, we employed
348 physiological analysis of the auditory system in mice and gerbils for assessing the potential of
349 ChReef for energy-efficient optogenetic SGN stimulation.

350 First, we studied optogenetic stimulation at the levels of SGN population as well as of individual
351 SGNs and cochlear nucleus neurons in C57B/6J mice 3-10 weeks after early postnatal

352 intracochlear injection of AAV2/9 carrying ChReef or ChRmine. Expression of both ChR variants
353 under the control of the human synapsin promotor was found in approximately 75% of the SGNs
354 (Fig. 4b) and line profile analysis confirmed targeting to the cell membrane (Fig. 4c). Optically
355 evoked auditory brainstem responses (oABR, Fig. 4a-g) were elicited in all mice upon stimulation
356 with green (522 nm, optimal excitation) and orange (594 nm) light delivered by a laser-coupled
357 optical fiber to the cochlea. oABR energy thresholds of ChReef expressing mice (Fig. 4g, 522 nm:
358 170 ± 120 nJ, n = 10 vs. 270 ± 240 nJ, n = 10 for ChRmine; p = 0.127, *t-test*) were a magnitude
359 lower than the previously reported lowest threshold found with f-Chrimson[18] (1.500 ± 100 nJ, p
360 < 0.0005). ChReef oABR thresholds were significantly lower than those for ChRmine for longer
361 wavelength light (594 nm, 1.250 ± 1070 nJ, n=16 vs. 2.450 ± 1.160 nJ, n = 13; p = 0.004, t-test)
362 relevant for future clinical oCI. Next, we investigated the potential of ChReef for optogenetic
363 restoration of auditory function in two mouse models of deafness: i) acute ototoxic (kanamycin)
364 ablation of hair cells and ii) genetic disruption of otoferlin, a synaptic protein essential for
365 synaptic sound encoding[38]. oABR thresholds and latencies remained unaltered in both models
366 (Fig. 4g, S18). To evaluate the temporal fidelity of optogenetic SGN stimulation, we recorded
367 oABRs in response to green (522nm) and orange (594nm) light pulses at different stimulation
368 rates (1 ms, 10 mW, Fig. 4i) and pulse durations (Fig. 4h). oABR amplitudes declined with
369 increasing stimulation rate, whereby ChReef showed detectable oABRs to stimulation rates up to
370 100 Hz compared to 50 Hz for ChRmine. Both ChReef and ChRmine enabled oABRs in response
371 to 20 µs-long durations of green light pulses whereby the duration eliciting the maximal P1-N1
372 oABR amplitude was shorter for ChReef (Fig. 4i: 200 µs for ChReef vs. 600 µs).

373

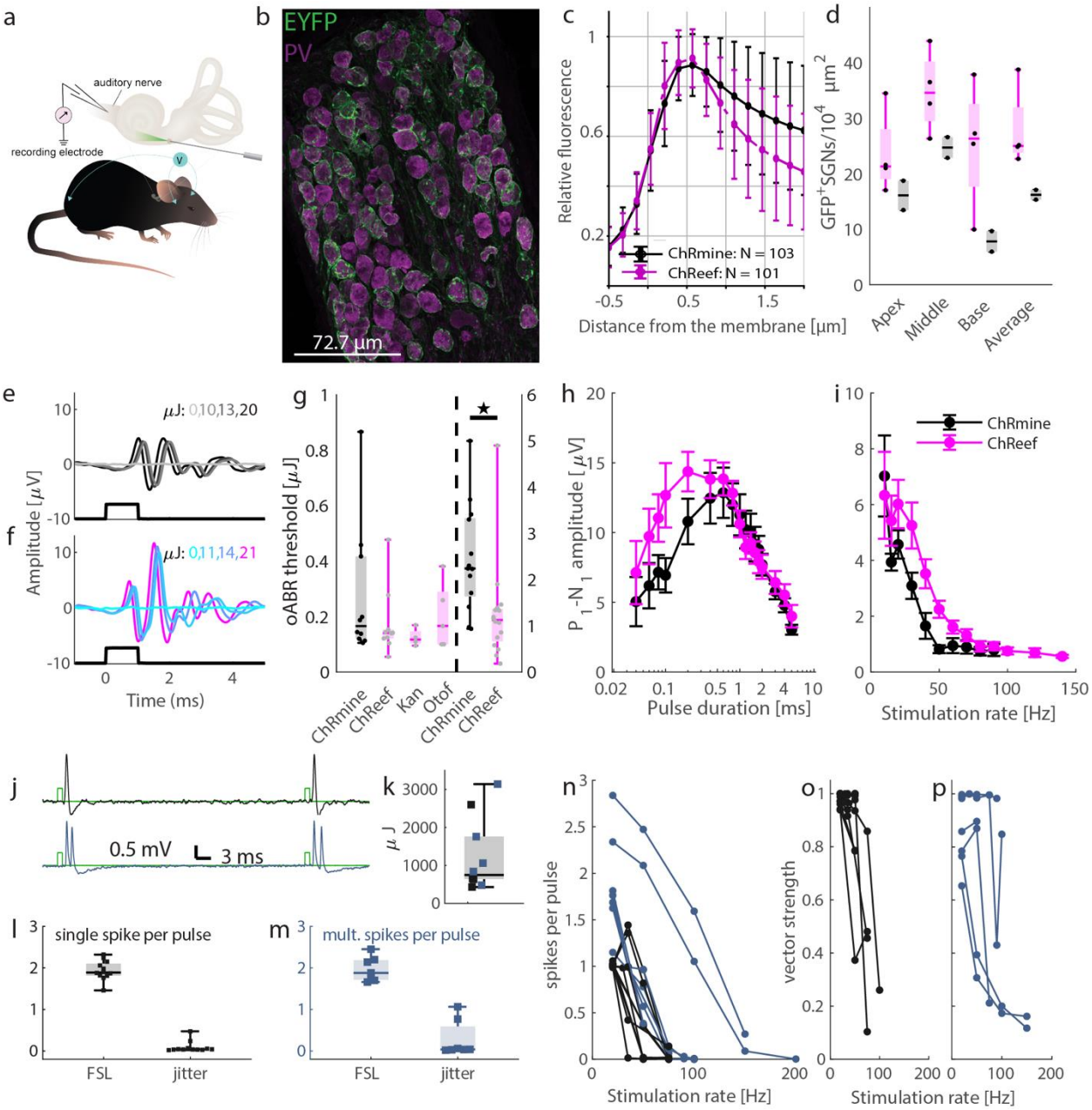

Figure 4. ChReef-mediated optogenetic stimulation of the mouse auditory nerve has low light requirements and acceptable temporal fidelity. a, Schematic representation of optical auditory brainstem recordings (oABR) and juxtacellular recordings from single putative spiral ganglion neurons (SGNs). **b**, Mid-modiolar cochlear slice at the apical turn displaying SGN transduction (Parvalbumin - magenta) and transduction (GFP - green). **c,** Line profile analysis in single SGNs for ChRmine and ChReef expressing SGN- Relative GFP fluorescence of ChRmine and ChReef transduced SGNs by the distance from the cellular membrane. **d**, Density of GFP positive cells across all cochlear turns for ChRmine (black) and ChReef (magenta) injected mice. **e,f**, exemplary traces for oABRs driven with varying radiant flux (1 ms pulses at 10 Hz, colors code the radiant energy in µJ) for exemplary mice injected with AAV2/9-hSyn-ChReef-ES-EYFP-TS (**e**) or AAV2/9-

385 hSyn-ChRmine-ES-EYFP-TS (**f**). **g**, Energy threshold of oABRs for ChReef (magenta) and ChRmine
386 (black) using both 522 nm (left panel, data presented on separate axis) and 594 nm (right panel)
387 light: center line: mean, box: median, error bars: 75 percentile, n=15 mice for ChReef and n=12
388 mice for ChRmine (*p = 0.004, t-test). **h**, P1-N1 amplitudes of oABRs for varying pulse durations
389 using ~10 mW pulses at 10 Hz (mean ± SD). **i**, P1-N1 amplitudes of oABRs at varying repetition
390 rates using 1 ms, 10 mW pulses (mean ± SD) with 522 nm (ChReef: magenta; ChRmine: black). **j**,
391 Exemplary responses of SGNs to 1ms, ~6mW pulses at 20Hz illustrating two SGN response
392 categories: single spike responding (<=1.1spikes per pulse, black) and multiple spike responding
393 SGNs (>1.1 spike per pulse, blue). **k**, Energy threshold of individual SGNs and median threshold
394 (n=10, criteria: spike per pulse > 0.005, vector strength > 0.3). **l,m**, Median of first spike latency
395 and first spike jitter for single spike (n=11) and for multiple spike (n=7) responding pSGNs. **n, o,**
396 Spike probability and vector strength of single spike and multiple spike responding SGNs at
397 varying stimulation rates (samples size as in l, m).

398

399 To further scrutinize the temporal SGN response to ChReef-mediated optogenetic stimulation
400 (1ms, 6 mW, 20Hz, delivered as for oABR), we turned to *in vivo* recordings from single 'putative
401 SGNs' (here forth coined SGNs)[18,39,40] (Fig. 4a). Approximately two-thirds of the SGNs responded
402 with a single spike and the other third with multiple spikes (mostly 2-3 but some with more tonic
403 discharge, Fig. 4j, l-n), reminiscent of responses of CatCh-expressing SGNs in Mongolian gerbils[41].
404 Single SGN energy thresholds (Fig. 4k, < 2.000 nJ) tended to be higher than oABR thresholds but
405 still much lower than all previously reported values (>6.000 nJ, for f-Chrimson, vf-Chrimson and
406 Chronos[40,42]). First spike latency and first spike latency jitter were comparable among the two
407 SGN groups (Fig. 4l, m). Next, we studied spike probability and spike synchronization with the
408 stimulus (vector strength) as a function of stimulation rate for both SGN groups (Fig. 4n-p).
409 Consistent with the oABR, many SGNs failed to reliably follow stimulus rates beyond 50 Hz (Fig.
410 4i). Both, recordings of oABRs and single SGNs entailed optogenetic stimulation over several
411 hours without obvious loss of responsiveness along the experiment. Finally, we performed patch-
412 clamp recordings of optogenetically (green-light) driven synaptic transmission from ChReef-

413 expressing SGNs to bushy cells in acute slices of the cochlear nucleus (Fig. S20). Excitatory
414 postsynaptic recordings were reliably evoked for rates of optogenetic stimulation ≤50 Hz.

415 To assess the potential of ChReef for future optogenetic hearing restoration, we measured the
416 spectral spread of excitation in the cochlea, a limiting factor of eCIs. We performed
417 multielectrode array recordings of multi-unit activity in the inferior colliculus (IC[35], Fig. 5a, Fig.
418 S22) of Mongolian gerbils in response to green light (522 nm) elicited either by an optical fiber or
419 LED-based multichannel cochlear implants[43]. Following postnatal cochlear injection of AAV-
420 PHP.S-hSyn-ChReef (Fig. 5b, Fig. S21), we recorded ChReef-mediated oABRs and moved on to IC
421 recordings in gerbils with low oABR thresholds (215.5 ± 153 nJ, *n*=10, Fig. S22). The energy
422 threshold for 1 ms light stimuli to elicit multi-unit activity in the IC (d'prime of 1) amounted to
423 101 ± 73 nJ for optical fiber stimulation (*n* = 10) and 238.5 ± 235 nJ when stimulating with single
424 LEDs (531 nm, 11 LEDs in n=2 gerbils, Fig 5c, Fig. S24c). The temporal fidelity of multi-unit activity
425 (Fig. S23) was consistent with results obtained in mouse SGNs (Fig. 4). The spread of excitation
426 with fiber and LED stimulation was comparable to the natural hearing, i.e. found with pure tones
427 (Fig.5d-g, Fig. S24d). We found a clear shift of the center of excitation when addressing LEDs of
428 different tonotopic positions (Fig. S24a, b). We then turned to ototoxic deafening confirmed with
429 recordings among acoustic stimulation (Fig 5c, S22e). The energy threshold for 1 ms light stimuli
430 to elicit multi-unit activity (i.e. a d'prime of 1) amounted to 345.4.6 ± 349 nJ (Fig. 5c) and the
431 spectral spread remained comparable (Fig. S24d).

432 In an effort to further evaluate the potential of ChReef for clinical translation, we turned
433 to the common marmoset as a non-human primate model (Fig. 5h). AAV.PHP.eB-hSyn-ChReef
434 along with kanamycin was administered into the left cochlea of mature marmosets from a

micropump via a microcatheter inserted into scala tympani via the round window from a posterior tympanotomy. In order to ensure efficient administration of the viral suspension and to avoid cochlear pressure build up, a vent was generated next to the stapes footplate or by stapes removal rupturing the oval window membrane.

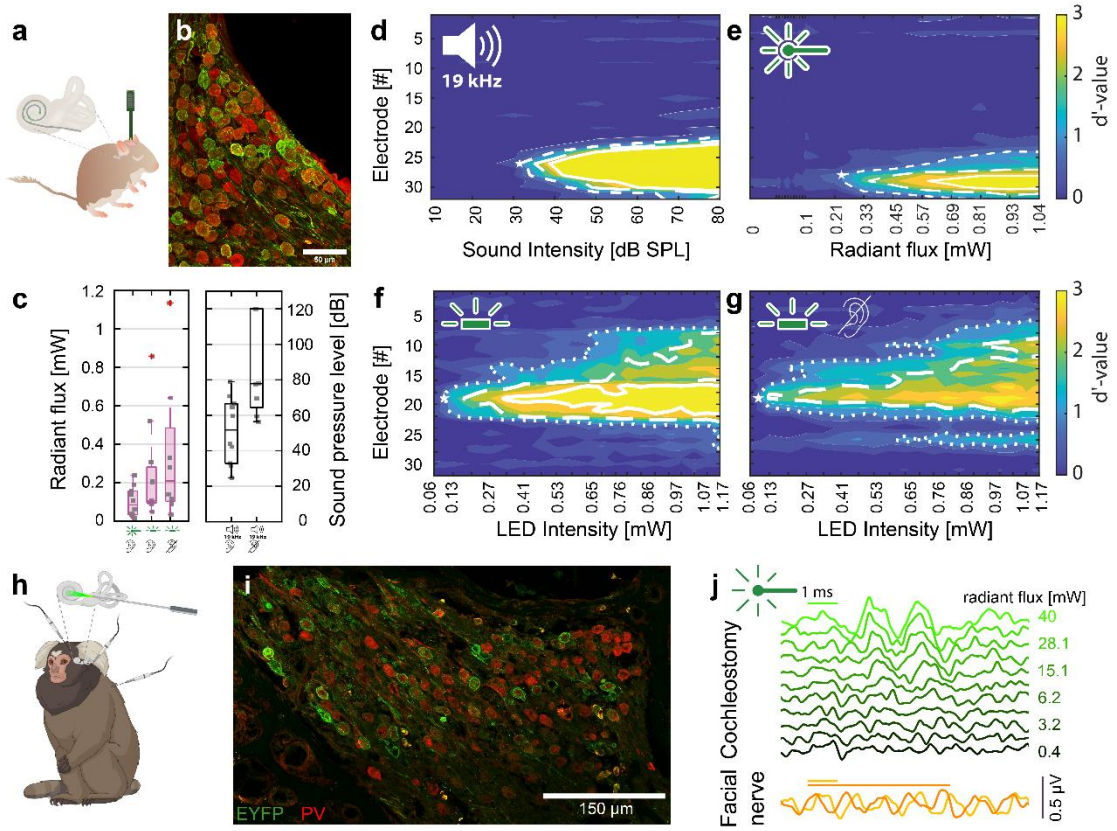

Figure 5: Characterizing the optogenetic activation of the auditory pathway by inferior colliculus recordings in Mongolian gerbil and ABR in the Common marmoset

a, Schematic of experimental setup. **b**, Example image of gerbil cochlea showing ChReef (GFP; green) expression in spiral ganglion neuron (parvalbumin; red). Scale bar 50 µm. **c**, Neuronal thresholds computed as level eliciting a d' of 1. Type of stimulation from left to right: optical fiber (522 nm); LED; LED after deafening; acoustic stimulation at 19 kHz prior and after deafening. **d-g,** Exemplary spatial tuning curves (STC) for different stimulus modalities: 19 kHz stimulation (d), laser pulses delivered via optical fiber (e), optical stimulation delivered by single LED prior (f) and after deafening (g). White stars indicate the electrode with the smallest intensity to reach d' of 1 (best electrode). **h**, Schematic of experimental setup for marmosets. **i**, Confocal imaging of

450 ChReef expression in the apical turn of the left cochlea. 30% of SGNs identified with parvalbumin
451 (red) weakly expressed eYFP. **j**. oABR recordings in a common marmoset resulting in successful
452 activation of the auditory pathway. An optical fiber emitting green light (525 nm, top panel) was
453 inserted through a cochleostomy enlargening the round window niche. Auditory responses were
454 observed from 4.7 mW, with 1 ms long pulses while no responses were found even with 43 mW
455 green light pointing directly at the facial nerve with pulses of 1 and even 5 ms duration (bottom
456 panel).

457

458 11 weeks (75 ± 19 days; means ± SD) later we tested for oABRs to green light stimulation from an
459 optical fiber placed into the round window and cochleostomies (Fig. S25a, b). This way, we could
460 demonstrate first proof of concept for optogenetic hearing in one out of nine marmosets (Fig.
461 5j). No responses were elicited by directly illuminating the neighboring facial nerve with green
462 light at maximally possible radiant fluxes. Histological examination revealed substantial ChReef
463 expression in SGNs of the treated (left) cochlea in three out of nine animals (expression rate: 33
464 % [oABR positive], 23.3 % and 0.7 % SGN [oABR negative]). None of the SGNs across all turns of
465 the right cochlea were positive (Fig. S25). Immunohistochemical analysis of whole mounts of the
466 organ of Corti revealed near complete loss of hair cells on the kanamycin injected side (Fig. S26).
467 Together, these data prove the principle of nano-Joule and sustained optogenetic stimulation of
468 the rodent and primate auditory pathway, capitalizing on the higher single-channel conductance,
469 longer open times, and sustained photocurrents of ChReef

470

471

472 **Discussion**

473 ChReef is a new optogenetic actuator for sustained optogenetic control of excitable cells enabling
474 firing rates of up to 50-100 Hz with nano-Joule light requirements which we expect to facilitate a
475 wide range of optogenetic applications. Combining good membrane targeting, higher single

476 channel conductance, moderate open times, and low photocurrent desensitization, ChReef
477 enabled breakthroughs in three different optogenetic applications: Efficient red-light
478 optogenetic excitation block of CMs, optogenetic vision restoration at low light intensities, and
479 lowering the energy threshold for optogenetic activation of the auditory pathway by one order
480 of magnitude. The closing kinetics of ChReef (~30 ms deactivation time constant) provide a good
481 match to the temporal fidelity required for optogenetic control of cardiomyocytes and retinal
482 ganglion cells. For the auditory system, the temporal fidelity of SGN stimulation was inferior to
483 that observed with ultrafast ChRs such as f-Chrimson, vf-Chrimson and Chronos (deactivation
484 time constants of 3, 1.5, and <1 ms at body temperature, respectively)[14,18,40,42]. Current eCI
485 coding strategies employ high stimulation rates (~1 kHz) for sampling the envelope of the sound
486 signal. However, good speech understanding was obtained at much lower rates (from 20 Hz[44]) in
487 the range achievable by ChReef-mediated SGN stimulation (up to ~100 Hz). Nonetheless, future
488 efforts should aim for generating ChReef variants with faster closing kinetics to enhance the
489 temporal fidelity of optogenetic stimulation and to shift the absorption to longer wavelengths
490 for better alignment with red-light laserdiode-based medical devices such as optical cochlear
491 implants. Moreover, enhancing target cell specific expression of ChReef variants by developing
492 optimal combinations of capsids and promoters and derisking the transgene by removing the
493 fluorescent tag remain important objectives for future studies prior to clinical translation.

494 **Material and Methods**

495 **ChR variant generation**

496 The humanized DNA sequence, coding for *Rl*CCR1-309 (*Rhodomonas lens ChR*, also called
497 ChRmine, accession number: MN194599[10,45]), C-terminally fused to TS-EYFP-ES was cloned into
498 the mammalian expression vector pcDNA3.1 (−) (Invitrogen, Carlsbad, USA). The previously
499 described targeting sequences of the inward rectifying potassium channel Kir2.1 (TS and ES) were
500 employed for optimized plasma membrane expression[8,13,14]. The mutations F219Y, T218L and
501 S220A were introduced into ChRmine by site-directed mutagenesis using the primers shown in
502 Supplementary Table 3.

503 The pcDNA3.1(-) derivatives carrying the humanized DNA sequences of Chronos-EYFP
504 (*Stigeoclonium helveticum* ChR, accession number: KF992040[46]), ChR2-EYFP (C-terminally
505 truncated variant Chop2-315 of ChR2 from *Chlamydomonas reinhardtii*, accession number:
506 AF461397[47]), CatCh-EYFP (ChR2 L132C), Chrimson-EYFP (*Chlamydomonas noctigama* ChR,
507 accession number: KF992060[46]) and f-Chrimson-EYFP (Chrimson Y261F/S267M[40]) were kindly
508 provided by Ernst Bamberg (MPI of Biophysics). The humanized DNA sequence, coding for *Co*ChR
509 (*Chloromonas oogama* ChR, accession number: KF992041[46,48], Addgene plasmid #59070), C-
510 terminally fused to EGFP and the humanized DNA sequence, coding for *Gt*CCR4 (*Guillardia theta*
511 ChR 4, accession number: MF039475.1[48,49]), C-terminally fused to EYFP, were cloned into the
512 mammalian expression vector pcDNA3.1 (−) (Invitrogen, Carlsbad, USA). The humanized DNA
513 sequence, coding for *Gt*CCR2 (*Guillardia theta* ChR 2, accession number: XM_005841372 [49]) C-
514 terminally fused to EYFP, cloned into the mammalian expression vector pcDNA3.1 (−) were
515 obtained from Addgene (plasmid # 159121). The previously described ChR variants ChR2 T159C[18],
516 ChRmine Y260F[9] and *Co*ChR H94E/L112C/K264Tv[50] were generated by site-directed mutagenesis
517 using the primers shown in Supplementary Table 3.

518

519

520

521 ***In vitro* measurements**

522 **Cell culture and transfection**

523 The manual patch-clamp recordings of ChR variants were conducted in the neuroma glioblastoma
524 cell line NG108-15 (ATCC, HB-12377TM, Manassas, USA) cultured in Dulbecco's Modified Eagle
525 Medium (DMEM, Sigma, St. Louis, USA) supplemented with 10 % fetal calf serum (Sigma, St.
526 Louis, USA) and 1 % penicillin/streptomycin (Sigma, St. Louis, USA) (supplemented DMEM:
527 $DMEM^+$) at 37 °C and 5 % CO_2. Cells were seeded on 24-well plates one day prior to transfection
528 by Lipofectamine with pcDNA3.1(-) derivatives carrying the aforementioned ChR variants at a
529 NG108-15 cell confluency of 50-70 %. For each well, a transfection mix of 100 µl DMEM, 3 µl
530 Lipofectamine LTX (Invitrogen, Carlsbad, USA) and 500 ng of the pcDNA3.1(-) derivatives was
531 prepared and added to a well with 400 µl of $DMEM^+$. Twenty-four hours after transfection the
532 medium was exchanged against 500 µl $DMEM^+$ supplemented with 1 µM all-trans retinal.

533 For automated patch-clamp recordings, HEK293T cells (DSMZ, Braunschweig, Germany)
534 or NG108-15 (ATCC, HB-12377TM, Manassas, USA) cells were seeded in a T75 culture flasks or 6-
535 well plates and allowed to grow for one day before transfection. The cells were seeded at a
536 density of 16 thousands cells/cm^2 in $DMEM^+$ (initial concentration before adhesion 80 thousands
537 cells/ml). For noise analysis experiments transfection of HEK293T cells was done in T75 flasks.
538 Immediately prior to transfection, the media was replaced with 12 mL of OptiMEM
539 (ThermoFisher, Waltham, Massachusetts, U.S.) with 1.25 µM all-trans-retinal (Sigma, St. Louis,
540 MO, U.S.). Then, 19.5 µg of plasmid DNA and 78.1 µg of polyethyleneimine (PEI, Polysciences,
541 Warrington, PA, U.S.) were separately dissolved in 1.5 ml of OptiMEM (ThermoFisher, Waltham,
542 Massachusetts, U.S.) each. The DNA and PEI solutions were then combined and incubated for 15

543 minutes at room temperature. The resulting DNA/PEI mix was added to the cells and incubated
544 at 37°C and 5% CO_2 for 4 hours. After transfection, the media in the flask was changed back to
545 DMEM$^+$ supplemented with 1 µM all-trans-retinal. The cells were then incubated at 37°C and 5%
546 CO_2 for 40 hours prior to the automated patch-clamp experiment. For all other experiments with
547 automated patch-clamp transfections of HEK293T or NG108-15 cells were done in 6-well plates
548 without prior media exchange. For each well 2.5 µg of plasmid DNA and 7.5 µg of PEI were
549 separately dissolved in 0.2 ml of OptiMEM. The DNA and PEI solutions were then combined and
550 incubated for 15 minutes at room temperature. The resulting DNA/PEI mix was added to the
551 wells of 6-well plate and incubated at 37°C and 5% CO_2 for 16 hours. After transfection, the media
552 in the flask was exchanged to new DMEM$^+$ supplemented with 1 µM all-trans-retinal. The cells
553 were then incubated at 37°C and 5% CO_2 for 28 hours prior to the automated patch-clamp
554 experiment.
555
556 **Manual patch-clamp recordings and data analysis**
557 The electrophysiological characterization of the ChR variants was conducted by whole cell patch-
558 clamp recordings of transiently transfected NG108-15 cells at membrane potential of -60 mV, if
559 not stated differently. Cells were patched two days after transfection under voltage-clamp
560 conditions using the Axopatch 200B amplifier (Axon Instruments, Union City, USA) and the
561 DigiData1322A interface (Axon Instruments, Union City, USA). Patch pipettes with a resistance of
562 2-6 MΩ were fabricated from thin-walled borosilicate glass on a horizontal puller (Model P-1000,
563 Sutter Instruments, Novato, USA). The series resistance was <15 MΩ. The bath solution contained
564 140mM NaCl, 2mM $CaCl_2$, 2mM $MgCl_2$, 10mM HEPES, pH 7.4; and the pipette solution contained

565 110mM NaCl, 2mM $MgCl_2$, 10mM EGTA, 10mM HEPES, pH 7.4. All recordings were performed at
566 room temperature (20°C). Light pulses were applied by a fast computer-controlled shutter
567 (Uniblitz LS6ZM2, Vincent Associates, Rochester, USA) using diode-pumped solid-state lasers
568 focused into an optic fiber (d=400 µm). The open-source statistic software "R" as well as Origin
569 9.0 (OriginLab, Inc., Northampton, MA, USA) and GraphPad Prism (GraphPad Software, La Jolla,
570 CA, USA) were employed for data analysis.

571 The photocurrents of the ChRmine variants were measured in response to green light pulses
572 (λ=532 nm) of varying duration with a saturating intensity of 23 mW/mm^2. The photocurrents of
573 Chronos, Catch and ChR2 T159C were measured upon the application of blue light pulses (λ=473
574 nm) of varying duration with a saturating intensity of 31 mW/mm^2. The stationary current
575 densities ($J_{-60\ mV}$) of the ChRmine variants were calculated as the quotient of the mean stationary
576 current upon stimulation with a 2 s light pulse and the capacitance of the cell. The stationary
577 current densities ($J_{-60\ mV}$) of Chronos, Catch and ChR2 T159C were calculated as the quotient of
578 the mean stationary current upon stimulation with a 0.5 s light pulse and the capacitance of the
579 cell. To avoid an experimental bias, cells were chosen for the recordings independent of the
580 brightness of their fluorescent signal.

581 The stationary-peak-ratio of the photocurrents of the ChRmine variants was calculated as the
582 quotient of the mean stationary current upon stimulation with a 2 s light pulse and the peak
583 current. The peak recovery of the ChRmine variants was assessed by photocurrent recordings
584 upon illumination with two subsequent 3 s light pulses with a varying time between the light
585 pulses (Δt between pulses, ms, ranging from 50 to 3350 ms). Peak recovery was calculated as the
586 quotient of the difference between the peak and stationary current of pulse two (I_{p2}-I_{s2}) and peak

587 and stationary current of pulse one (I_{p1}-I_{s1}) in %. The time constant of the peak recovery (τ_{peak-}
588 $_{recovery}$) was determined by a fit of the quotient of the difference between the peak and stationary
589 currents of two subsequent 3s light pulses at saturating intensity to a monoexponential function.

590 The light intensity dependence of the stationary photocurrent of the ChRmine variants was
591 investigated by photocurrent measurements upon illumination with 2 s light pulses (λ=532 nm).
592 The EC_{50} values were determined by hyperbolic fitting. For ChRmine wt the fitting range was
593 thereby restricted to the range, which could be approximated by a hyperbolic function. The light
594 intensity dependence of ChRmine wt was furthermore fitted to an equation corresponding to a
595 steady state minimal kinetic model describing a substrate inhibition of the partial type [15]:
596

$$I = I_{max} \frac{\left(1 + \frac{E}{K_i} R_c\right) E}{\left(1 + \frac{E}{K_i}\right) E + K_a} \qquad \text{[Equation 1]}$$

597 I: stationary photocurrent, I_{max}: maximal stationary photocurrent if $K_i \rightarrow \infty$, E: irradiance, R_c:
598 effective ratio of single channel currents (i_1/i_2), K_a: effective equilibrium constant for light
599 dependent closed (C) to open transitions (O1), K_i: effective equilibrium constant for light
600 dependent transitions between open states (O1/O2). The light intensity dependence shown in
601 Figure 1 was fitted with the following parameters: K_a=0.021±0.005, K_i=0.062±0.029,
602 R_c=0.47±0.05. Although the informative value of the fitted parameters is limited due to the
603 absence of a more detailed description of the ChRmine photocycle, which could serve as a basis
604 for a precise kinetic model, the fit demonstrates that the light intensity dependence of the
605 stationary photocurrent of ChRmine resembles a substrate inhibition of the partial type.

606 The τ_{off} values of all shown ChR variants were determined by a fit of the decaying
607 photocurrent elicited in response to a 3 ms light pulse to a monoexponential function. In order
608 to investigate the dependence of the off-kinetics on the membrane potential τ_{off} values were
609 determined at membrane potentials ranging from -120 mV to +60 mV.

610 The action spectra of the ChRmine variants were determined by peak current recordings in
611 response to ns-light-pulses of wavelengths ranging from 430 to 590 nm with pulse energies at
612 the different wavelengths set to equal photon counts of $5*10^{18}$ photons/m^2 using the Opolette
613 355 tunable laser system (Opotek Inc, Carlsbad, USA).

614 **Automated patch-clamp recordings and data analysis**

615 The automated patch-clamp recordings were done using Syncropatch 384 (Nanion, Munich,
616 Germany) equipped with prototype illumination units. The Syncropatch 384 robot was operated
617 using the Biomek v2.1 software. The data was acquired using the PatchControl v2.1 software.
618 The cells that were transfected were washed twice with DPBS (ThermoFisher, Waltham,
619 Massachusetts, U.S.) and then treated with 3 ml of TrypLE (ThermoFisher, Waltham,
620 Massachusetts, U.S.) at 37°C for 7 minutes (HEK293T) or 15 minutes (NG108-15). After the TrypLE
621 treatment, 3 ml of standard external solution was added to the cells and incubated at 4°C for 5
622 minutes. The standard external solution was composed of 140 mM NaCl, 4 mM KCl, 2 mM $CaCl_2$,
623 1 mM $MgCl_2$, and 10 mM HEPES, with pH adjusted to 7.4 using NaOH. The osmolarity of the
624 solution was set to 298 mOsm by adjusting the concentration of glucose. The cells were then
625 resuspended by pipetting and centrifuged at 200 g for 10 minutes, and the supernatant was
626 discarded. Finally, the cells were resuspended in 10 mL of Standard External Solution.

627 To begin, the S-type chip (Nanion, Munich, Germany) was filled with 80 µl per well of
628 Divalent-Free solution, and the chamber's bottom was subsequently filled with Internal solution.
629 The Divalent Free solution contained 140 mM NaCl, 4 mM KCl, and 10 mM HEPES, with pH
630 adjusted to 7.4 using NaOH. The osmolarity of the solution was set to 289 mOsm by adjusting the
631 concentration of glucose. The Internal solution was composed of 10 mM NaCl, 10 mM KCl, 110
632 mM KF, 10 mM HEPES, and 10 mM EGTA, with pH adjusted to 7.2 using KOH. The osmolarity of
633 the solution was set to 285 mOsm by adjusting the concentration of glucose. Next, 20 µl per well
634 of solution was removed, and 20 µl per well of detached cells were introduced to the chip. The
635 cells were then captured by a suction pulse of -200 mbar for 5 s, followed by consecutive suction
636 pulses of -50 mbar for 1 min. Subsequently, the voltage was decreased incrementally from 0 mV
637 to -100 mV in steps of 25 mV while maintaining the cells under a pressure of -50 mbar HEK293T)
638 or -80 mbar (NG108-15). After this, 20 µl per well of solution was removed from the chip, and 40
639 µl per well of seal enhancer solution was added. The seal enhancer solution contained 130 mM
640 NaCl, 4 mM KCl, 10 mM $CaCl_2$, 1 mM $MgCl_2$, and 10 mM HEPES, with pH adjusted to 7.4 using
641 NaOH. The osmolarity of the solution was set to 302 mOsm by adjusting the concentration of
642 glucose. The chip then underwent three wash steps, during which 40 µl of solution was removed
643 from each well and replaced with 40 µl per well of standard external solution (unless another
644 extracellular solution composition is specified). After the second wash step, two suction pulses
645 of -220 mbar were applied for 2 s each to establish a whole-cell configuration for HEK293T cells
646 or three suction pulses of -350 mbar were applied for 5 s each to establish a whole-cell
647 configuration for NG108-15 cells. After completing all of the procedures described, the remaining
648 volume of solution in the wells was 100 µl. To illuminate the cells during the planar patch clamp

649 experiment, a specialized illumination unit was utilized. The unit consists of 96 LEDs (Lumileds
650 Luxeon Z, Schiphol, Haarlemmermeer, The Netherlands) that are coupled to light fibers. During
651 the experiment, the end of the fiber is submerged under the solution and positioned 7 mm from
652 the cell being measured. The illumination units with LEDs of different colors were used in the
653 planar patch-clamp experiments: green LEDs (λ_{max} = 530 nm, LXZ1-PM01), blue LEDs (λ_{max} = 470
654 nm, LXZ1-PB01), orange LEDs (λ_{max} = 590 nm, LXZ1-PL02) and red LEDs (λ_{max} = 632 nm, LXZ1-
655 PD01). To regulate the intensity of light used in each measurement, the forward current of the
656 illumination unit was adjusted. The intensity was measured directly at the output of the light
657 fibers using a bolometer (Coherent OP-2 VIS, Santa Clara, California, U.S.). The intensity of light
658 was specified for each type of measurement.

659 The data collection for the noise analyses of both types started with measurement of
660 photocurrent dependence on the membrane voltage (IV curve). The range of voltages was from
661 -120 mV to 60 mV with equidistant 20 mV steps. Each sweep was separated into three
662 consecutive steps, with 2 s in the dark, 2 s under the illumination of a saturating intensity for the
663 stationary photocurrents of the measured ChRs (4 mW/mm^2 for ChReef and ChRmine; 6
664 mW/mm^2 for CatCh) and 1 s in the dark. This data was used to calculate the reversal potentials,
665 which were used to determine the electrochemical potentials on the membranes. This step was
666 followed by different protocols and data treatment procedures for stationary and non-stationary
667 analyses. The data treatment encompassed a thorough selection of recordings that met our strict
668 quality control criteria, followed by the processing of the selected raw traces using our
669 proprietary Python library and custom scripts developed in-house.

670 For stationary analyses, all cells were held at a voltage of -100 mV or -60 mV. 40
671 consecutive pairs of sweeps, 6.5 s long each, were recorded at a sampling rate of 20 kHz. Each
672 pair of sweeps was followed by 25 s of non-recorded waiting time in the dark. The first sweep of
673 each pair had a 6-second illumination pulse at an intensity of 0.4 mW/mm^2 (0.6 mW/mm^2 for
674 CatCh), and the second sweep was recorded under dark conditions.

675 Sweeps suitable for stationary noise analysis were selected based on the following
676 criteria. Basic parameters of the seals were assessed for each sweep, and only sweeps with a seal
677 resistance over 1 GΩ, a membrane capacitance lower than 50 pF, and a series resistance below
678 20 MΩ were used for further analysis. The parameters of the dark noise were then assessed using
679 parts recorded under the dark conditions for the sweeps with data recorded under illumination
680 conditions. Sweeps with a root mean square deviation (IRMS) of dark currents over 5.5 pA were
681 disregarded. The stability of the noise was assessed by dividing the dark part of the current into
682 100 pieces, calculating IRMS in all of them, and disregarding sweeps with a standard deviation of
683 IRMS over 0.3 pA. The recorded sweeps were grouped back into pairs of consecutive traces that
684 were recorded under light and dark conditions. Only those pairs with stationary photocurrents
685 over 200 pA during the interval from 2 to 6 s after turning on the illumination were considered.
686 Cells that had four or more pairs of traces remaining after applying all of the aforementioned
687 quality control criteria were selected for stationary noise analysis. For each pair, the interval from
688 2 to 6 s was taken. The sweep recorded under the light conditions was fitted to a double
689 exponential function, and the resulting fit was subtracted from the sweep. A mean current was
690 subtracted from the sweep recorded in the dark. After these corrections, the power spectral
691 density (PSD) was calculated for both sweeps. The differences between the PSD under the light

692 and dark conditions were determined and then averaged for each cell. The averaged difference
693 PSDs were then fitted to the single Lorentzian function in a range from 2.5 to 25 Hz. This allowed
694 for the determination of the corner frequency and the difference PSD at 0 Hz (f_c and S_0
695 correspondingly as in eq. 2). Open probabilities of the channels (P_o) were then determined for
696 each cell, taking into consideration their relation (eq. 3) to corner frequency and off kinetics
697 (where τ_{off} was determined from the single exponential fit of the photocurrent decrease after
698 turning off the light). Only cells whose difference PSD met the criteria of 1 Hz < f_c < 15 Hz and 0 <
699 P_o < 1 were considered in the determination of the single channel conductance values.

700

$$S(f) = \frac{S_0}{1 + \left(\frac{f}{f_c}\right)^2} \qquad \text{[Equation 2]}$$

$$1 - P_o = \frac{1}{2\,\pi f_c \tau_{off}} \qquad \text{[Equation 3]}$$

701

702 The variances σ^2 of the noise associated with the opening and closing of the ChRs were
703 determined by utilizing the obtained values of f_c and S_0 (eq. 4). The unitary photocurrents were
704 subsequently calculated by applying the relation between the mean and variance in the binomial
705 distribution (eq. 5) to the mean net stationary current I and σ^2. Afterwards, the unitary
706 photocurrents were converted to single channel conductances by dividing them by the
707 electrochemical potential gradient.

$$\sigma^2 = \frac{\pi\, f_c\, S_0}{2} \qquad \text{[Equation 4]}$$

$$i = \frac{\sigma^2}{I\,(1 - P_o)} \qquad \text{[Equation 5]}$$

708

709 In the non-stationary analysis, 300 sweeps were recorded for each cell at the holding
710 voltage of -100 mV or -60 mV. At -100 mV each sweep had a 5 ms illumination step at an intensity
711 of 14 mW/mm^2 forward current so that recordings are done close to single turnover conditions,
712 preventing protein from going to the putative second open state upon absorption of a second
713 photon. At -60 mV each sweep had an illumination step of 150 ms at an intensity of 0.4 mW/mm^2.
714 After each illumination step the dark currents were recorded for 5 s.

715 The non-stationary noise analysis involved several steps to select the suitable sweeps for
716 analysis. Firstly, basic parameters of the seals were assessed, and only those sweeps that met the
717 following criteria were used: seal resistance over 1 GΩ, membrane capacitance lower than 50 pF,
718 and series resistance below 20 MΩ. Sweeps with root mean square deviation (IRMS) of dark
719 currents over 4.5 pA were disregarded. Only cells with a peak photocurrent over 500 pA (over
720 100 pA for -60 mV traces) were considered. To minimize possible unwanted effects of the
721 photocurrent rundown, only the sets of at least 50 consecutive recordings (25 recordings for -60
722 mV traces) with negligible rundown of the peak photocurrent (lower than 1 pA/sweep) were
723 considered and the variance of the photocurrent was determined as a half of the average of the
724 squared differences between pairs of consecutive recordings. The dependence of the variance
725 on the photocurrent value was then fitted linearly to determine the unitary photocurrent as a

726 proportionality factor (eq. 6) and the background current variance as the free term (σ_b^2, squared
727 IRMS at photocurrent of 0 pA). Finally, any cells that had linear fits indicating σ_b smaller than 4
728 pA were excluded from the analysis, since none of the recordings showed such a low IRMS value
729 based on its direct calculation in the dark current. The remaining cells were used to compute the
730 single channel conductance.

$$\sigma^2 = P_o(1 - P_o)Ni^2 + \sigma_b^2 \approx P_o Ni^2 + \sigma_b^2 = I \cdot i + \sigma_b^2 \qquad \text{[Equation 6]}$$

731 The photocurrents of the ChR variants at a membrane voltage of -60 mV were measured in
732 response to green LED pulses (λ=530 nm) for ChRmine variants and GtCCR4, or blue LED pulses
733 (λ=470 nm) for CatCh, CoChR, CoChR-3M, and GtCCR2. Light pulses of 2 s duration with a
734 saturating intensity (green LED at 5.6 mW/mm² and blue LED at 8.3 mW/mm²) were used to
735 determine photocurrent densities and desensitization kinetics. The stationary photocurrent
736 densities of the ChR variants were calculated as the quotient of the mean stationary photocurrent
737 upon stimulation with a 2 s light pulse and the capacitance of the cell. Due to the lack of a
738 fluorescence control, we selected only cells with peak photocurrents greater than 20 pA. To avoid
739 bias that could inflate the apparent mean value of photocurrent density for small photocurrent
740 variants, cells with photocurrent densities in the lowest 15% were excluded for each variant.
741 Desensitization kinetics were determined by fitting the decays of the photocurrents from their
742 peak to stationary levels to a biexponential function. Normalized values for fast and slow
743 components' amplitudes were calculated as quotients of the corresponding amplitudes and the
744 sum of the two amplitudes.

745 Light pulses of 5 ms duration with an intensity of 13.0 mW/mm² for the green LED (ChRmine
746 variants, GtCCR4) and 19.3 mW/mm² for the blue LED (CatCh, CoChR, CoChR-3M, and GtCCR2)
747 were used to determine off-kinetics. The τ_{off} values of all ChR variants were determined by fitting
748 the decaying photocurrent elicited in response to a 5 ms light pulse to a monoexponential
749 function. To determine τ_{off} for CoChR, only cells with stationary photocurrent densities lower
750 than 50 pA/pF were selected to avoid effects of intracellular proton accumulation affecting pH-
751 dependent off-kinetics. To investigate the dependence of the off-kinetics on the membrane
752 potential, τoff values were determined at membrane potentials ranging from -120 mV to +60 mV.

753 For intensity dependence experiments, light pulses of 2 s duration were used for green light
754 (λ=530 nm) and orange light (λ=590 nm), while light pulses of 4 s duration were used for red light
755 (λ=632 nm). The intensity of light was regulated by adjusting the forward current of the
756 respective illumination unit. Alternating between fixed and variable light intensities was
757 employed to control for photocurrent rundown effects. The stationary photocurrents recorded
758 at varying intensities were normalized against preceding and subsequent measurements at fixed
759 intensities. The resulting dependencies for each recorded cell were fitted to hyperbolic functions
760 and normalized by their respective amplitudes from the fits. The normalized dependencies were
761 then averaged between the cells.

762 For the determination of relative ion permeability, photocurrents of ChRmine and ChReef in
763 response to green LED pulses (λ=530 nm) of 2 s duration were measured at different voltages,
764 and reversal potentials were determined. Permeability ratios were calculated according to the
765 Goldman–Hodgkin–Katz equation. To assess the relative permeability of potassium ions relative
766 to sodium (PK/PNa), we measured photocurrent at voltages ranging from -120 mV to +60 mV in

767 10 mV steps and assessed reversal potential shifts after exchanging the standard intracellular
768 solution (KF-based) with a NaF-based intracellular solution containing 10 mM NaCl, 10 mM KCl,
769 110 mM NaF, 10 mM HEPES, and 10 mM EGTA, with pH adjusted to 7.2 using NaOH. A reverse
770 exchange of the intracellular solution was performed to account for reversal potential drift. The
771 shift in reversal potential due to the solution exchange was calculated as the difference between
772 the reversal potential in the NaF-based intracellular solution and the average of the two reversal
773 potentials measured in the KF-based intracellular solution (before exchange and after reverse
774 exchange). Cells with a reversal potential drift greater than 5 mV were excluded from the analysis.

775 To assess the relative permeability of calcium ions relative to sodium (PCa/PNa), we measured
776 photocurrent at voltages ranging from -120 mV to +60 mV in 10 mV steps and assessed reversal
777 potential shifts after extracellular solution dilution, which changed the NaCl concentration from
778 [NaCl]_ini = 140 mM to [NaCl]_fin = 11 mM and the $CaCl_2$ concentration from [$CaCl_2$]_ini = 2.5
779 mM to [$CaCl_2$]_fin = 83 mM. An additional series of extracellular solution dilutions was performed
780 to return sodium and calcium concentrations to their initial values to account for reversal
781 potential drift. The shift in reversal potential due to the solution exchange was calculated as the
782 difference between the reversal potential in the Ca-based extracellular solution and the average
783 of the two reversal potentials measured in the Na-based extracellular solution (before dilution
784 and after reverse dilution series). Cells with a reversal potential drift greater than 10 mV were
785 excluded from the analysis.

786 To assess the relative permeability of protons relative to sodium (P_H/P_{Na}), we measured
787 photocurrent at voltages ranging from -121 mV to 59 mV in 3 mV steps. The permeability of
788 protons relative to sodium was calculated from the photocurrent reversal potential using a

789 standard intracellular solution and an NMG-based extracellular solution containing 90 mM
790 NMDG, 3.2 mM NaCl, and 10 mM MES, with pH adjusted to 6.4 using HCl.

791 Data analysis was performed using our proprietary Python library and custom scripts developed
792 in-house.

793 ***Ex vivo* and *in vivo* experiments – General**

794 **rAAV purification and cloning of constructs for *ex vivo* and *in vivo* experiments**

795 Viral vector purification procedure was performed as previously published[14] and an extensive
796 description is available in ref.[51]. In brief, triple transfection of HEK-293T cells was performed using
797 the pHelper plasmid (TaKaRa, USA), trans-plasmid with either the AAV2/9, PHP.eB or PhP.S
798 capsid[52] and cis-plasmid with either ChRmine or ChReef under the control of human synapsin or
799 CAG promotor. Cells were regularly tested for mycoplasma contamination. Viral particles were
800 harvested cells and medium; precipitated from medium with 40% polyethylene glycol 8000
801 (Acros Organics, Germany) in 500mM NaCl and combined with cell pellets for processing. Pellets
802 were suspended in 500mM NaCl, 40mM Tris, 2.5mM MgCl2, pH 8, and 100 Uml−1 of salt-
803 activated nuclease (Arcticzymes, USA) at 37 °C for 30 min. Cleared lysates were purified over
804 iodixanol (Optiprep, Axis Shield, Norway) step gradients (15%, 25%, 40%, and 60%) at 350,000 ×
805 g for 2.25 h. rAAV containing fractions were concentrated using Amicon filters (EMD, UFC910024)
806 and formulated in sterile phosphate-buffered saline (PBS) supplemented with 0.001% Pluronic F-
807 68 (Gibco, Germany). Viral vector titers were determined by the number of DNase I resistant vg
808 using AAV titration kit (TaKaRa/Clontech) by qPCR (StepOne, Applied Biosystems) according the
809 manufacturer's instructions or with adaptations to usage in crystal digital PCR (dPCR) system.

810 Here, dilutions of purified vector DNA were subjected to crystal dPCR using 5x Naica PCR reaction
811 mix (Stilla, R10056) supplemented with primers provided in the AAV titration kit, 0,8mg/µl Alexa
812 647 (Invitrogen, 11570266) and 1.5x Eva Green (Biotum, #31000-T). Formation of droplet crystals
813 and PCR was performed in a Naica Geode (Stilla) using Naica Ruby or Sapphire Chips (Stilla) and
814 finally analyzed in the Naica Prism3 reader (Stilla) equipped with Crystal Reader and Crystal Miner
815 softwares (Stilla). rAAVs titers and quantification method used is indicated for each rAAV in the
816 respective methods chapter. Purity of produced viral vectors was routinely checked by silver
817 staining (Pierce, Germany) after gel electrophoresis (Novex™ 4–12% Tris–Glycine, Thermo Fisher
818 Scientific) according to the manufacturer's instruction. Viral vector stocks were kept at −80 °C
819 until injection. In summary, final constructs used for gene therapy in rodents consisted of
820 ChRmine (mice) or ChReef (mice, gerbils and marmosets) under control of the human synapsin
821 (neuronal targeting) or CAG promoter (cardiac cluster stimulation) tagged with enhanced yellow
822 fluorescent protein (eYFP) with enhancement of trafficking signal (TS) and ER export signal (ES)
823 packed into PHP.eB for vision restoration experiments, for stimulation of the auditory pathway:
824 AAV2/9 for mice and or PHP.S for gerbils and PHP.eB for marmosets, and in AAV2/9 for cardiac
825 cell cluster stimulation.

826

827 **Animals**

828 All animal experiments were carried out in compliance with the relevant national and
829 international guidelines (European Guideline for animal experiments 2010/63/EU) as well as in
830 accordance with German laws governing animal use. The procedures have been approved by the

831 responsible regional government office. Rodents were kept in a 12h light/dark cycle with ad
832 libitum access to food and water.

833 **Preparing neonatal mouse cardiomyocytes**

834 Hearts were explanted from p0-p3 mice killed by decapitation and directly placed on ice cold PBS.
835 Remaining tissue and atria were carefully removed, and ventricular cardiomyocytes (CMs)
836 isolated with the neonatal heart dissociation kit for mouse and rat (Miltenyi, Germany). 1.5 – 2
837 million cells were plated on a 6-well-plate coated with 10 µg/ml fibronectin (Sigma; F1141-5MG)
838 and maintained in IMDM (GlutaMAX, no phenol red; Gibco 21056-023) supplemented with 10%
839 FBS superior (Sigma; S0615) and 1% Penicillin/Streptomycin (Life Technologies; 15140122) in
840 standard cultivation conditions (37°C, 5% CO_2). One day later, medium was exchanged to reduce
841 FBS to 0.5% and AAV transduction was performed with AAV2/9-CAG-ChRmine-TS-EYFP-ES with
842 $1.1x10^{10}$ GC/ml (qPCR) and AAV2/9-CAG-ChReef-TS-EYFP-ES with $6x10^{10}$ GC/ml (qPCR)
843 corresponding to ~226 and ~69vp/cell, respectively. On day 3, the cells were dissociated and
844 plated on Ø 10 mm round coverslips in CM clusters compromising 50.000 cells within 15 µl locally
845 on an 8 µl 0.1% gelatine drop. Cells were incubated in this small drop for 20 min to build cardiac
846 clusters and afterwards medium filled up in the well. After 1-2 days CM cluster started to beat
847 spontaneously and 0.5% FBS IMDM medium was exchanged every 2-3 days.

848 **Preparing hiPSC-derived cardiomyocytes**

849 Human CMs were differentiated from the induced pluripotent stem cell line UMGi014-A clone 2,
850 which was created from dermal fibroblasts from a male donor using integration-free Sendai virus
851 and was described previously. CMs differentiation and purification involved WNT signaling

852 modulation and lactate-based metabolic selection as described previously[53,54]. Differentiated
853 CMs were cryopreserved for further use. For measurements, 1.5 – 2 million cells were thawed
854 and plated on a 6-well-plate coated with 16 mg/mL Geltrex (Thermo Fisher Scientific; A1413302)
855 and maintained in CM culture medium (RPMI 1640 medium (GlutaMAX; Thermo Fisher Scientific;
856 72400054), B27 (Thermo Fisher Scientific; 1750404) supplemented with 2 mM thiazovivin
857 (Sigma-Aldrich; 420220-10MG), at 37°C and 5% CO2. Medium was replaced after two days to
858 remove residues of thiazovivin and changed every 2-3 days afterwards. AAV transduction was
859 performed with MyoAAV-CAG-ChRmine-TS-EYFP-ES with ~$1x10^{11}$ GC or MyoAAV-CAG-ChReef-
860 TS-EYFP-ES with ~$1.8x10^{10}$ GC (CdPCR). Four days after transduction, cells were dissociated and
861 plated on Ø10 mm round coverslips in cardiac cell clusters comprising 50.000 cells within 8 µl
862 drop on a Geltrex/DMEM/Ham's F-12 coated area. Cells were incubated in this drop for 40
863 minutes to build cardiac clusters and afterwards medium was filled up with CM culture medium.
864 After two days cardiac clusters started to beat spontaneously. Medium was replaced every 2-3
865 days.

866 **Analysis of optogenetically evoked contraction of CM clusters**

867 Experiments with beating CM clusters were performed between day 3 and 5 after plating for the
868 neonatal CMs and after 3-7 days for the hIPSC-derived CMs with continuous perfusion with
869 Tyrode solution (comprising 140 mM NaCl, 5.4 mM KCl, 1.8 mM $CaCl_2$, 2 mM $MgCl_2$, 10 mM
870 glucose, and 10 mM HEPES; pH 7.4, adjusted with NaOH) to keep the cells at approximately 35 °
871 C. Electrical stimulation (0.2 ms long biphasic pulses, 45 V for neonatal CMs and 25 V for hiPSC-
872 derived CMs) was performed with two platinum electrodes and the Myostim stimulator
873 (Myotronic, Germany) and light stimulation with a LedHub (Omicron). 510 nm light was

874 generated by a 500 – 600 nm LED, filtered through a ET500/20 excitation filter and reflected onto
875 the cells via a 561 nm beamsplitter (AHF, F38-561). 630 nm light was generated with the 625 LED
876 through a 635/18 excitation filter and reflected onto the cells via a 409/493/573/652
877 beamsplitter (AHF, F68-409) within an inverted IX73 microscope and through a 20x objective
878 (LUCPLFLN20XPH/0,45). Imaging light was filtered by a 780 nm long pass filter (Schott RG780) to
879 avoid excitation of ChRmine and ChReef by the illumination and images were taken with a UI-
880 306xCP-M camera (iDS, Germany) and analysed online with the custom made Myocyte online
881 Contraction Analysis (MoCA) software recently described in detail48 giving the absolute average
882 of motion vectors per frame |V| as output through NI 9263 CompactDAQ (NI, Austin, U.S.)
883 recorded with Powerlab 8/35 and LabChart 8.1.16 software for analysis. The software and
884 Powerlab were also used to trigger electrical pacing and LEDs. Light intensity was calibrated with
885 the S170C sensor and Powermeter (Thorlabs, Germany). To determine the threshold of optical
886 pacing, CM clusters were illuminated by ten consecutive light pulses (5 ms for 510 nm; 50 ms for
887 630 nm in neonatal CMs and 5 ms for 630 nm in hIPS derived CMs) with the indicated repetition
888 rates. Light intensity was lowered stepwise to the light intensity at which pacing capability was
889 lost. The lowest intensity capable to trigger contractions 1:1 with the last 8 of 10 light pulses was
890 defined as pacing threshold. Excitation block was tested during supramaximal electrical pacing
891 (0.2 ms long biphasic pulses, 45 V for neonatal CMs and 25 V for hiPSC-dervied CMs) at a
892 repetition rate 0.5 Hz above the spontaneous beating frequency or with 1 Hz if no spontaneous
893 beating was observed. 5 s long light pulses were used, and excitation block defined as successful,
894 when electrical stimulation failed to induce any detectable contraction during the illumination
895 period.

896 **Histology for cardiomyocytes**

897 Neonatal heart cells as well as hiPSC-derived CMs were fixed in 4% formaldehyde for 20 min,
898 permeabilised with 0.2% Triton X100 for 20 min and stained in DPBS (Sigma; D8537)
899 supplemented with 5% donkey serum for 2 h with primary antibodies against cardiac troponin I
900 (ab47003, Abcam: 1:800) and for 1 h with secondary antibodies conjugated with Cy5 (711-175-
901 152, JacksonLab, U.S., 1:400) diluted in DPBS with 1:1000 DAPI (0018860.01, Th.Geyer) at room
902 temperature. Images of single CMs for analysis of expression rate were taken through a 10x
903 (10X/NA 0,4 Olympus UPLSAPO) or 20x objective (20x/NA 0,7 Olympus UCPLFLN PH) with an IX83
904 inverted fluorescence microscope equipped with an ORCA-flash 4.0 digital camera (C11440,
905 Hamamatsu Photonics) and the MT20 illumination system as light source controlled via the
906 CellSens® software. Acquisition of images was performed with following filter settings: 387/11
907 excitation, 410 beamsplitter and 440/40 emission for DAPI, 485/20, 504 and 525/30 for eYFP,
908 560/25, 582, and 684/24 for Cy5. Transduction rate was calculated by the percentage of eYFP
909 positive cells among all CMs identified by cardiac troponin I antibody-staining.

910 CM clusters were imaged with a LSM 800 confocal microscope (Zeiss) equipped with
911 spectral multi-alkali photomultiplier detectors. Z-stack acquisition was performed using a Plan-
912 Apochromat 20x/0.8 M27 via the ZEN 2.6 (blue edition) software (Zeiss) with a pinhole of 55 µm
913 for Dapi, 24 µm for eYFP, 27 µm for the red channel and 31 µm to image Cy5. Pictures were post-
914 processed using stack correction (Background+Decay+Flickr), extended depth of focus (Wavelets,
915 highest Z-Stack Alignment) and Image calculator (subtraction of autofluorescence) of the Zen 3.4
916 (blue edition) software.

917 **Statistics of optogenetic stimulation of CM clusters**

918 All dots represent the individual result from one CM cluster and the mean is shown with the
919 standard error of the mean as bars. Statistical analysis was performed with a 2-way ANOVA with
920 Holm-Sidak multiple comparison test for the optical pacing, unpaired students t-test for the
921 excitation block with 510 nm as well as for the expression rate, and Fisher´s exact contingency
922 test for the defibrillation capability with 630 nm.

923 **Methods for optogenetic stimulation of the visual system**

924 **Intravitreal injection**

925 All *in vivo* electrophysiological experiments were carried out in compliance with the relevant
926 national and international guidelines (European Guideline for animal experiments 2010/63/EU)
927 as well as in accordance with German laws governing animal use. The procedures have been
928 approved by the responsible regional government office. Rodents were kept in a 12h light/dark
929 cycle with ad libitum access to food and water.

930 3-months old female and male Rd1 (C3HeB/FeJ, JAX 000658) mice were anesthetized with a
931 subcutaneous injection of a fentanyl (0.05 mg/kg), midazolam (5 mg/kg), and medetomidine (0.5
932 mg/kg) (FMM) cocktail. Mice were then secured using a bite bar and placed on top of a
933 temperature controller (Supertech) to maintain a body temperature of 37°C. For local anesthesia
934 of the eyes, eye drops containing 0.5% Proxymetacain were applied and hydration gel (Bayer,
935 Bepanthen) was placed on the eyes to prevent dryness whenever possible. Before injection, a
936 hole posterior to the ora serrata was created using a 27-gauge needle. Then, a Hamilton syringe
937 was guided through this hole into the intravitreal space and 2µl of virus solution of PHP.eB-hsyn-

938 ChRmine-TS-EYFP-ES (1,89x10^{13} GC/ml, dPCR) or PHP.eB-hsyn-ChReef-TS-EYFP-ES (8,59x10^{13}
939 GC/ml, dPCR) was injected at 4µl/min using a motorized injector (Stoelting). After 5 min the
940 syringe was withdrawn and the anesthesia was reversed with a subcutaneous injection of a
941 naloxone (1.2 mg/kg), flumazenil (0.5 mg/kg), and atipamezole (2.5 mg/kg) cocktail.

942 **Optical stimulation**

943 For visual stimulation at different light intensities, a LED (530 nm, Thorlabs, M530L4) in
944 combination with a filter wheel and 6 different neutral density filters (Thorlabs, FW1AND) was
945 used. Light intensities were measured using a digital optical power and energy meter (Thorlabs,
946 PM100D). Green light was presented to the contralateral eye from a distance of 2 cm while the
947 eye ipsilateral to the recording site was covered. Visual stimulation was timed (200 ms at 1 Hz)
948 using a pre-programmed pulse generator (Doric, OTPG_8), which was synchronized with the
949 electrophysiological recordings. Accordingly, for visual stimulation using a screen, white full field
950 flashes (200 ms at 1 Hz) were presented using PsychoPy[55] on an iPad screen (LG LP097QX1) 5 cm
951 from the contralateral eye. A photodiode was used to synchronize the visual stimulation with the
952 electrophysiological recordings.

953 **Electrophysiological recordings**

954 Three to four weeks after intravitreal virus injections, electrophysiological measurements were
955 performed. To enable stable fixation in the recording setup, a head-post was implanted onto the
956 skull of vision restored mice at least 5 days before electrophysiological recordings using standard
957 surgical procedures. To record neural activity, 32-channel silicon probes (Cambridge NeuroTech,
958 type H10b) with a 32-channel headstage (Intan technologies, C3324) were connected via a SPI

959 interface cable (Intan technologies, C3216) to an USB interface board (Intan technologies,
960 C3100). Data was recorded at 20 kHz using RHX software. Mice were anesthetized using FMM
961 cocktail and head-fixed in a holding tube. The head of the mouse was aligned in all three axes to
962 the coordinate system of the probe manipulator. Openings in the skull above the primary visual
963 cortex (AP: 3.9 mm, ML: 2.1 mm) were created using a drill, and the probe was lowered into V1
964 at a speed of 2 µm/s. Data was acquired at different depths (DV: -0.4 mm to -0.8 mm below the
965 brain surface) in both hemispheres during separate recordings and stimulation of the
966 contralateral eye. Electrophysiological recordings were performed 10 min after reaching the
967 desired depth. CM-Dil (Thermo Fisher, CellTracker) was applied to the probe prior to brain
968 insertion to allow post-hoc confirmation of the recording site.

969 **Analysis of neural responses to optogenetic stimulation of the visual system**

970 Electrophysiological recordings were analyzed using kilosort3[56], and spike sorting results were
971 manually curated using the phy software (https://github.com/cortex-lab/phy). Only units with
972 stable responses across the duration of the session and high kilosort quality scores were included
973 in subsequent analysis. To obtain continuous firing rate estimates, single unit responses were
974 binned with a bin size of 1 ms and convolved with a gaussian kernel with a standard deviation of
975 10 ms. Trial-averaged responses were normalized to the mean and standard deviation of the
976 baseline (400ms before stimulus onset) across all intensities. Units that did not respond to the
977 highest light intensity were excluded (mean normalized firing rate during the stimulus smaller
978 than 2.58). The Gramm toolbox[57] was used to visualize raster plots. For significance testing across
979 time points a permutation based method[58] was used as described[59]. Briefly, using unpaired t-
980 tests differences between the two conditions for each time point are determined and

981 subsequently time clusters are identified using the bwconncomp.m function in Matlab (4
982 connected components). Time cluster significance is determined by comparison the t-statistics
983 of the actual data against the t-statistics of shuffled data (10000 permutations with randomized
984 labels).

985 **Histology and imaging after optogenetic stimulation of the visual system**

986 To visualize retinal expression patterns, eyes of vision restored animals after the
987 electrophysiological experiments were collected and fixed in 4% PFA for 1h at RT. After washing
988 in PBS, retinas were prepared and fixed again for 10 min in 4% PFA at RT. Fixed and washed
989 retinas were put in 30% Sucrose and subjected two three rounds of freezing and thawing on dry
990 ice. Then retinas were incubated for 1h in 10% normal donkey serum (NDS) and subsequently in
991 primary antibody solution (rabbit-GFP (Proteintech, 50430-2-AP), 1:666 in PBS with 3% NDS and
992 0.5% Triton-X) for 4 days at 4°C. After incubation, retinas were washed in PBS and incubated in
993 secondary antibody overnight at 4°C (AlexaFluor 488 (Invitrogen, A32970), 1:500 in PBS with 3%
994 NDS and 0.5% Triton-X). Finally, washed retinas were mounted in DAPI-containing Vectashield
995 (Vector Laboratories, H-1200).

996 For post-hoc analysis of recording sites, brains were collected and incubated in 4% PFA at 4°C
997 overnight. Then brains were washed and embedded in 4% agarose. 100µm coronal slices were
998 cut using a vibratome (Leica microsystems, VT1000S) and stained for 2h at RT (DAPI, Thermo
999 Fisher Scientific, D1306, 2.5 µg/ml). Washed brain slices were mounted on microscope slides in
1000 Vectashield (Vector Laboratories, H-1200).

1001 Images were captured using a Leica TCS SP8 laser scanning confocal microscope with 63×/ 20x oil
1002 immersion or a 10× air objectives (Leica Microsystems). Images were merged and processed
1003 using LAS X (Leica Microsystems) and Adobe Photoshop software.

1004 **Behaviour experiments for vision restoration in mice**

1005 Mice were maintained on a standard 12hr light/dark cycle, in ventilated and humidity-controlled
1006 racks, at room temperature. Mice of both sexes were used and experiments were performed
1007 during the daytime (corresponding to the mouse's subjective nighttime). All procedures related
1008 to the behaviour experiments were performed in accordance with the Canadian Council on
1009 Animal Care and approved by the Montreal Neurological Institute's Animal Care Committee.

1010 ***In vivo* epifluorescence imaging of the retina**

1011 As there is some variability across mice in the success of intravitreal injections, 3 weeks following
1012 intravitreal injections we performed a screen of fluorescence expression in their retina. Mice had
1013 to show clear YFP expression in their fundus images when viewed under an epifluorescence
1014 microscope (Phoenix Micron IV) to be selected to undergo behavioral testing with the light-
1015 room/dark-room test.

1016 **Light-room/dark-room test**

1017 The test environment consisted of two custom-made 30 cm x 30 cm x 85 cm rooms built from
1018 black corrugated plastic. Both rooms had a lid, which housed four white-light LED arrays (YM E-
1019 Bright). The light intensity on the floor of the light-room was 120 µW (measured with Thorlabs
1020 S130C, set to 530nm). There was a small opening between the two rooms to allow a mouse to

1021 pass from one room to the other. Experiments were performed three weeks after intravitreal
1022 injection. Since we have found that, for blind rd1 mice, a subset of them spent all their time in
1023 the room they start the trial in, which could bias results (for instance, if they started in the dark-
1024 room, and spent all their time there, it might look like they are sighted), for each trial we started
1025 mice in the light-room. Furthermore, to ensure that any preference for a room had to do with
1026 the lighting conditions, and not a preference for a specific one of the rooms independent of
1027 lighting conditions, we studied room preferences across four trials, switching which room was lit
1028 between trials. All trials were performed on the same day. The first trial last for 10 minutes and
1029 was considered habituation and was not used for analysis. Trials 2-4 lasted for 15 minutes each
1030 and were analyzed and averaged together. We recorded the mouse's position with an overhead
1031 camera (Logitech C270 HD) in the light-room. Analysis was performed in Bonsai [60], which was set
1032 up to detect the presence or absence of the mouse in the light room.

1033

1034 **Optogenetic stimulation of auditory pathway in rodents**

1035 **Postnatal AAV injection into the cochlea in mice and Mongolian gerbils**

1036 The same injection approach was performed for all animals which later would be subject to
1037 either: auditory brainstem recordings, juxtacellular recordings from single putative SGNs, *ex vivo*
1038 acute slice electrophysiology in mice, or recordings from the inferior colliculus in Mongolian
1039 gerbils. AAV injections into the left ear were performed at postnatal day 6 in C57BL/6J wild-type
1040 or B6;129P2-Otof$^{tm1.1Erei}$ (MGI: 4950055 [61]) mice or at postnatal day 7.3 ± 1.3 days in Mongolian
1041 gerbils[18,51]. The right ear served as a non-injected control. In brief, mouse and gerbil pups were

1042 randomly selected for virus injections. Under general isoflurane anesthesia (5% for anesthesia
1043 induction, 1–3% for maintenance with frequent monitoring of the hind-limb withdrawal reflex
1044 and anesthesia adjustments, accordingly) and local xylocaine as well as buprenorphine (0.1
1045 mg/kg) and carprofen (5 mg/kg) administration for analgesia, the cochlea of the left ear was
1046 accessed via a retroauricular incision. Body temperature was maintained at physiological
1047 temperature. The cochlea was gently punctured using a quartz capillary pipette, which was kept
1048 in place to inject the virus of following titers:

1049 Mice: AAV2/9-hsyn-ChRmine-TS-EYFP-ES 5.1×10^{13} GC/ml (qPCR),

1050 AAV2/9-hsyn-ChReef-TS-EYFP-ES 3.1×10^{13} (qPCR) and 2.45×10^{13} GC/ml (dPCR)

1051 Gerbil: PHP.S-hsyn-ChReef-TS-EYFP-ES 5.25×10^{13}GC/ml (qPCR)

1052 After virus injection the tissue in the injection area was repositioned and the wound was sutured.
1053 Carprofen (5 mg/kg) was administered for analgesia the day after surgery.

1054

1055 **Optical stimulation of the auditory pathway in rodents *in vivo***

1056 The left cochlea was exposed by performing a retroauricular incision behind the pinna followed
1057 by a bullostomy, where the round window was visualized and punctured. For mice a 50 µm
1058 optical fiber coupled to a 594 nm (OBIS LS OPSL, 100 mW, Coherent Inc., Santa Clara, United
1059 States) or a 522 nm (Oxxius combined with a motorized Power Attenuator, Lannion, France)
1060 diode laser was used. For gerbils a 200 µm optical fiber was only coupled to the prior mentioned

1061 522 nm laser. Laser power was calibrated prior to each experiment using a laser power meter
1062 (Thorlabs PM100USB).

1063

1064 **Optically evoked auditory brainstem responses in mice and deafness models**

1065 Data were obtained from 40 adult C57Bl/6J wild-type mice of either sex (22 male, 18 female) 78.9
1066 ± 26.3 days after virus injection (see: postnatal AAV injection into the cochlea) mice were
1067 subjected to *in vivo* optical stimulation and recordings. For evaluation in deafness models, 4
1068 additional C57Bl/6J and 5 B6;129P2-Otof$^{tm1.1Erei}$ mice, all injected with ChReef-YFP, were
1069 subjected to the same type of recordings. For the kanamycin deafness model, the cochlea was
1070 deafened after confirming comparable intensity thresholds of ChReef to previous recorded mice
1071 by application of kanamycin (200 mg/ml). For this, kanamycin was delivered locally by inserting
1072 a microfile needle into the round window. It was left for approximately 7 minutes before
1073 additional measurements were performed to confirm deafness by absence of acoustically evoked
1074 auditory brainstem responses. Surgeries and measurements were performed under anesthesia
1075 using isoflurane (5% for anesthesia induction, 1–3% for maintenance with frequent monitoring
1076 of the hind-limb withdrawal reflex and anesthesia adjustments, accordingly) and analgesia by
1077 sub-cutaneous injections of buprenorphine (0.1 mg/kg body weight) and meloxicam (5 mg/kg
1078 body weight). Body temperature was maintained at 37°C using a custom-designed heat plate
1079 through all the procedures.

1080 Stimulus generation and delivery, as well as data acquisition was performed using a custom-
1081 written software (MATLAB, MathWorks, Natick, MA, United States) employing National

1082 Instrument data acquisition cards and a custom-build laser-controller. Recordings were
1083 conducted in a soundproof chamber (IAC Acoustics, IL, United States). Optically evoked ABRs
1084 (oABRs) and acoustically evoked ABRs (aABRs) were recorded by placing needle electrodes
1085 behind the pinna, on the vertex, and on the back of the anesthetized mice. The difference in
1086 potential between the vertex and mastoid subdermal needles was amplified using a custom-
1087 designed amplifier, sampled at a rate of 50 kHz for 20 ms, filtered (300–3000 Hz) and averaged
1088 across 1000 stimulus presentations. The ABR threshold was defined and determined as the
1089 lowest light or sound intensity for which one of the 3 waves was reliably visible. The latency of a
1090 given wave was defined as the time delay between the stimulus onset and the peak of the wave
1091 of interest. The amplitude was defined as the difference between the positive peak (P) and the
1092 negative through (N), of a wave of interest.

1093

1094 **Data analysis of optically evoked auditory brainstem responses in mice**

1095 The mouse ABR data was analyzed using custom-made Matlab software (The MathWorks, Inc.,
1096 Natick, MA, USA). Averages were expressed as mean ± standard deviation. For statistical
1097 comparison between two groups, data sets were tested for equality of variances (F-test) followed
1098 by two-tailed unpaired Student's t-test.

1099

1100 **Juxtacellular recordings from optically driven single putative SGNs in mice**

1101 Data were obtained from 3 adult mice in age between 163 and 307 days after AAV injection (see:
1102 postnatal AAV injection into the cochlea). Surgery was performed under general anesthesia by
1103 isoflurane (see Optically evoked auditory brainstem responses in mice). Body temperature was
1104 maintained at 37°C using a custom-designed heat plate through all the procedures.

1105 The experimental/ surgical procedure consisted of the following steps: 1) The left cochlea was
1106 exposed via a bullostomy and the round window membrane was visualized. The cochlea of all
1107 animals was acutely deafened, following application of kanamycin (200 mg/ml). 2) The optical
1108 fiber was placed in the round window niche (see methods, Optical stimulation *in vivo*). 3) After
1109 positioning the fiber or 10 minutes after kanamycin application, optically induced oABRs were
1110 recorded and their threshold was determined. 4) The optical fiber was taken out, and the animal
1111 underwent a tracheotomy procedure and was subsequently intubated. 5) The animal was
1112 positioned in a custom-designed stereotactic head holder. 6) The optical fiber was placed in the
1113 round window niche (see methods, Optical stimulation *in vivo*). 7) Following removal of the
1114 pinnae, the scalp was reflected and portions of the lateral interparietal and left occipital bone
1115 were removed. Next, the cerebellum was partially aspirated to expose the left semi-circular
1116 canal. A reference electrode was placed on the contralateral muscles behind the right ear and
1117 was constantly maintained in a moist state to ensure optimal contact. Utilizing the left semi-
1118 circular canal as a reference point, a micromanipulator (Luigs Neumann SM 10) was employed to
1119 insert a borosilicate glass capillary into the cochlear meatus (WPI 1B120F-4, length 100mm, OD
1120 1.5 mm, ID 0.84 mm). 8) The optical stimulus consisted of laser pulses with a duration of 1ms, a
1121 stimulation rate of 20 Hz, and radiant flux of 6 mW. Using the micromanipulator's step function,
1122 putative optically sensitive spiral ganglion neurons (SGNs) were identified. Action potentials were

1123 amplified using an ELC-03XS amplifier (NPI Electronic, Tamm, Germany), filtered (300–20000 Hz),
1124 digitized (National Instruments card PCIe-6323), analysed, and prepared for display using
1125 custom-written MATLAB (The MathWorks, Inc.) software.

1126

1127 **Data analysis of juxtacellular recordings from optically driven single putative SGNs in mice**

1128 In accordance with prior work[42], neurons were classified as 'putative SGNs' if they met the
1129 following criteria: i) they exhibited a monophasic and ii) positive waveform, iii) were recorded at
1130 a depth exceeding 1000 µm below the cerebellum surface, and iv) displayed a first spike latency
1131 of less than 3ms in response to a 1ms light pulse presented at 6mW. We detected the initial spike
1132 that followed each stimulus and calculated both its average latency and latency jitter,
1133 represented by the standard deviation of the first spike latency. Additionally, we computed the
1134 vector strength and spikes per pulse by examining the discharge rate starting 150 ms into the
1135 stimulus train and extending it for the entire 350 ms stimulation train. This analysis characterizes
1136 the neuronal discharge during the adapted state of the neuron. For estimating the light intensity
1137 threshold, the laser intensity was gradually lowered until there were no more time-locked
1138 responses during the adapted state of the neuron. This protocol was only completed for six
1139 recorded neurons.

1140

1141 ***Ex vivo* acute auditory brainstem slice electrophysiology**

1142 At the age of 20 – 23 days, two weeks after AAV injection (see: postnatal AAV injection into the
1143 cochlea), brainstem slices were prepared as previously described[62]. In brief, the brain was

1144 immediately immersed in ice cold cutting solution (Supplementary Table 4) and pinned, dorsal
1145 side down, on a wax stage. With the ventral side of the brainstem exposed, the meninges were
1146 removed with curved forceps and a mid-sagittal cut was performed using a straight razor,
1147 splitting the brain in two hemispheres. Scissors were used to cut between the cerebellum and
1148 the occipital lobe of each hemisphere in order to separate the hind-brain from the fore-brain.
1149 The two blocks of hind-brain, containing brain-stem and cerebellum, were glued with
1150 cyanoacrylate glue, (Loctite 401, Henkel) medial side down, on the stage of a Leica (Wetzlar,
1151 Germany) VT 1200 vibratome. The lateral side of both brain blocks was facing upwards and was
1152 facing towards the advancing blade. A vibration amplitude of 1.5mm was used and the blade was
1153 placed at the height of the cerebellar flocculus. Cerebellar tissue was sectioned at an advancing
1154 speed of 0.05 – 0.1 mm/s and discarded. Thereafter, a speed of 0.02mm/s was used to obtain
1155 150µm thick parasagittal slices of the cochlear nucleus. The slices were incubated in artificial
1156 cerebro-spinal fluid (aCSF, Table S4) for a total of 30 minutes in a 35°C water bath (Julabo,
1157 Seelbach, Germany), after which they were maintained in aCSF at room temperature (23 – 25 °C)
1158 until recording. The pH of both the cutting solution and the aCSF was adjusted to 7.4. The
1159 osmolarity was, in mOsm, 310 for the aCSF and 320 for the cutting solution. Both solutions were
1160 continuously aerated with carbogen (95% O_2, 5% CO_2). An EPSC10 USB patch clamp amplifier was
1161 used for all recordings and was driven by the Patchmaster Next software (HEKA Elektronik GmbH,
1162 Reutlingen, Germany). The sampling interval was set to 25µs and the filter at 7.3 kHz. For better
1163 visualization of the slice's cell layers and auditory nerve fibers (ANFs), differential interference
1164 contrast (DIC) microscopy was used on upright Olympus BX51WI microscope with a water
1165 immersion LUMPLFLN40XW objective (Olympus, Hamburg, Germany). All recordings were

1166 performed at near physiological temperature (33 – 35°C). The bath solution flowed through an
1167 inline solution heater (SC-20 with CL-200A controller; Warner Instruments, Hamden, CT, USA).
1168 The temperature of the solution was monitored by a thermistor placed between the opening of
1169 the inflow tube and the slice in the recording chamber.

1170 Borosilicate filamentous glass capillaries (GB150F, inner diameter: 0.86 mm, outer diameter: 1.50
1171 mm, length: 80 mm, Science Products GmbH, Hofheim, Germany) were used to pull patch
1172 pipettes on a P-1000 micropipette puller (Sutter Instruments Co., Novato, CA, USA). The
1173 resistance at the tip of the pipette was strictly 2 – 3 MΩ to avoid increases of the series resistance
1174 (R_s) over long recordings. The pipettes were filled with intracellular solution (details on Table S4),
1175 which additionally contained 1 mM of Alexa-568 (Invitrogen / Fisher Scientific, Schwerte,
1176 Germany). The pH of the solution was adjusted to 7.4 and its osmolarity to 325 mOsm, to prevent
1177 osmotic collapse of the patched neuron, preserve the cell's vigour and prevent fluctuations of
1178 the R_s over long recordings. Voltage clamp experiments were performed with a V_{hold} = -70 mV,
1179 corrected for a liquid junction potential of 12 mV. Only cells with R_s values less than 8 MΩ were
1180 included in the analysis. Afferent fiber optogenetic stimulation was performed using a green laser
1181 included in the Oxxius multi-wavelength bundle (LBX-488-40-CSB, maximum Power: 40 mW; LCX-
1182 532-50CSB, maximum power: 50 mW; OBIS-594-100, maximum power: 100 mW; LBX-638-100-
1183 CSB, maximum power: 100mW; Laser 2000 GmbH, Wessling, Germany). Synapses were driven
1184 with trains of stimuli yielding varying success rates of optically eliciting excitatory postsynaptic
1185 currents, hereafter termed oEPSC probability (P_{oEPSC}). P_{oEPSC} was defined as $\frac{Number\ of\ oEPSCS}{50}$, 50
1186 signifying the number if 1ms light pulses that were delivered to the ANF. Minimal stimulation
1187 irradiance was defined as the lowest value that could yield a P_{oEPSC} = 1 at 10 Hz. This irradiance

1188 value was used later in the experiment to assess the P_{oEPSC} at higher frequencies. For ANF
1189 stimulation, 5, 10, 20, 33, 40, 50 and 100 Hz were the tested frequencies. In direct transduction
1190 experiments, where the photocurrent properties of ChReef were measured, 10, 20, 30, 50, 100,
1191 200, 300 and 350 Hz were used instead. Electrophysiology data were analysed using Igor Pro
1192 (Wavemetrics, Lake Oswego, OR, USA). Evoked release was analysed using custom Igor scripts.
1193 Confocal z-stacks were processed with the NIH ImageJ software[63]. Figures were assembled for
1194 display using open-source vector graphic software Inkscape (https://inkscape.org).

1195

1196 **Immunohistochemistry and immunofluorescence imaging for acute slice electrophysiology**

1197 The 150 µm thick slices that were used for electrophysiological recordings were fixed for 30
1198 minutes in Formaldehyde (FA) at room temperature after the experiment. Afterwards they were
1199 washed in PBS for 10 minutes to halt fixation and blocked with GSDB for 1 hour at room
1200 temperature. After fixation the slides were kept for 10 minutes in ice cold PBS to halt fixation and
1201 then washed for 1 hour at room temperature in goat serum dilution buffer, which contained in
1202 16% normal goat serum, 450 mM NaCl, 0.3% Triton X-100, and 20 mM phosphate buffer (PB, pH
1203 7.4). The slides were then incubated in primary antibodies diluted in GSDB, for 3 hours, in a wet
1204 chamber at room temperature. Four washing steps followed, that lasted 10 minutes each, two
1205 of them with Wash Buffer (450 mM NaCl, 0.3% Triton X-100 and 20mM PB) and two more with
1206 PBS. The slides were then incubated with secondary antibodies overnight at 4°C and, afterwards,
1207 washed twice with Wash Buffer and twice more with PBS as before. Before mounting, the slides
1208 were maintained in 5mM PB for 10 minutes and were then mounted with a drop of Mowiol (Carl

1209 Roth GmbH, Karlsruhe, Germany) and covered with a thin glass coverslip. Double sided tape
1210 spacers of 120µm thickness were used for mounting to flank the slice before the application of
1211 Mowiol. This way, the coverslip's weight would not be applied fully on the slice, avoiding extra
1212 vertical pressure, which resulted in better preservation of structural integrity of the tissue.
1213 Immunofluorescence imaging was performed on a Zeiss LSM 780 Microscope with a 40x NA1.4
1214 *Oil* Plan-Apochromat objective. *Primary antibodies:* chicken-anti-GFP (1:500, Abcam, Berlin,
1215 Germany), guinea-pig-anti-vGLUT1 (1:1000, Synaptic Systems GmbH, Göttingen, Germany).
1216 *Secondary antibodies:* goat-anti-chicken 488 (1:200, Thermo Fisher Scientific, Waltham, USA)
1217 goat-anti-guinea-pig 568 (1:200, Thermo Fisher Scientific, Waltham, USA).

1218

1219 **Inferior colliculus recordings during optical stimulation of the cochlea in the Mongolian gerbil**

1220 Multi-channel recordings of neuronal clusters were performed in the tonotopically organized
1221 central nucleus of the inferior colliculus (IC) of Mongolian gerbils at the age of 82.9 ± 18.1 days;
1222 while stimulating SGNs optically or acoustically as previously described[35]. Briefly, a craniotomy
1223 was performed on the right hemisphere of the animal's skull to access the IC, contralateral to the
1224 injected ear. A linear 32-electrode silicon probe (Neuronexus, Ann Arbor, USA) was positioned
1225 above the brain ~2mm lateral to lambda and then was slowly inserted ~3.3mm into the brain
1226 (measured from the surface of visual cortex) using a micromanipulator. Mapping of recording
1227 sites was done using acoustic stimuli (Fig. S13) and the probe was further advanced (or retracted)
1228 accordingly. Recordings were performed using a Digital Lynx 4S recording system (Neuralynx;

1229 Dublin, Ireland) along with custom-built hardware, in combination with custom-written and
1230 established MATLAB software.

1231

1232 **Data analysis of inferior colliculus recordings**

1233 The recorded signal from the 32 channels was bandpass filtered between 600 and 6000 Hz,
1234 digitized and spike times were computed as any waveform crossing three times the mean
1235 absolute deviation of the signal (MAD). A one millisecond refractory period was included to not
1236 overestimate the spike count of the signal. Post-stimulus time histograms (PSTH) were computed
1237 by binning spike counts in 0.2 ms bins. The first three consecutive bins crossing threshold of 3x
1238 MAD indicate t_{on} and, respectively, the last three consecutive bins over threshold indicate t_{off}.
1239 Based on the time window extracted, the signal was further analyzed and sorted in a two-
1240 dimensional matrix according to stimulus intensity and corresponding recording site. From this
1241 matrix, we calculated the cumulative distribution index (d') based on spike rates calculated across
1242 increasing intensities starting with 0 intensity condition. This indicates a change/increase in the
1243 neuronal firing rate in relation to baseline levels i.e. a d' of 1 indicates an increase in firing rate
1244 of 1 standard deviation from baseline and distinguish triggered signals from noise[35]. Based on
1245 these computed matrices, iso-contour lines at integer d' values were constructed and minimums
1246 specify thresholds to d' indicated. A d' of 1 indicates an increase in firing rate of 1 standard
1247 deviation from baseline and distinguish triggered signals from noise[35]. Based on these computed
1248 matrixes, iso-contour lines at integer d' values were constructed and minimums specify
1249 thresholds to d' indicated.

To analyze temporal properties, activity obtained from responsive recording channels were extracted and channels reaching a d' of 1 when optically stimulating at 1 mW were analyzed further. To calculate the number of spikes per stimulus, we divided the spike counts recorded by the number of repeats per recording and by the number of pulses from stimulation rate used. To calculate the vector strength, a measure of spike timing relative to stimulation cycle the following formula was employed as previously[41]:To analyze temporal properties, responsive recording channels were extracted and channels reaching a d' of 1 when optically stimulating at 1 mW were analyzed further. To calculate the number of spikes per stimulus, we divided the spike counts recorded by the number of repeats per recording and by the number of pulses from stimulation rate used To calculate the vector strength, a measure of spike timing relative to stimulation cycle the following formula was previously[41]:

$$VS = \frac{\sqrt{[\sum_{i=1}^{n} \cos \theta i]^2 + [\sum_{i=1}^{n} \sin \theta i]^2}}{n} \qquad \text{[Equation 7]}$$

With θ describing the spike timing computed from stimulus onset to following stimulus onset for a given stimulus cycle (phase). The Rayleigh test (eq. 8) was then performed in order to test the significance of vector strength for each unit and each repeat.

$$L = 2 * length(\theta i) * (VS^2) \qquad \text{[Equation 8]}$$

1267 If $L<13.8$, $p>0.001$ and vector strength significance is rejected and set to 0. Firing rates were
1268 computed across all recordings by dividing the spike counts recorded in the determined spike
1269 window by the duration of that spike window. These values were normalized to the highest firing
1270 rate recorded for plotting.

1271

1272 **LED-based multichannel cochlear implant calibration**

1273 LED based implants were assembled as previously described[43] but employing green CreeLEDs
1274 (531 nm). Prior to each experiment, optical implants were calibrated using custom-made
1275 software built with MATLAB (v2012a) and an integrating sphere (2P3, Thorlabs, Dachau,
1276 Germany). Each LED is calibrated individually using pulsed stimulation with 1 ms pulses from 0 to
1277 100% of maximum 10mA current provided by a current source generated with a custom-made
1278 system based on NI-DAQ-Cards (NI PCI-6229; National Instruments; Austin, US).

1279

1280 **LED-based multichannel cochlear implant stimulation**

1281 Upon careful insertion through the round window until the most proximal LED, LEDs were
1282 individually addressed using a custom-made system based on NI-DAQ-Cards (NI PCI-6229;
1283 National Instruments; Austin, US). To screen for optical intensity thresholds, each LED was
1284 individually stimulated from 0 to 20% of 10mA current at 1% steps and from 20% to 100% of
1285 10mA current at 10% steps.

1286

1287 **Deafening**

1288 Following the first set of recordings, the implant was left in place and a solution of 200 mg/ml
1289 kanamycin diluted in saline was injected carefully through the round window. The solution was
1290 left to sit for 15-30 minutes and following deafening confirmation from acoustic recordings, the
1291 experiment protocols were repeated.

1292

1293 **Brain histology**

1294 Following the end of the experiment, the animal was sacrificed under deep anesthesia via cervical
1295 dislocation and brains/cochleae were collected. Brains were left in 8% FA over a week and
1296 transferred to 30% sucrose for 24 hours. Brains were then carefully mounted using cryomatrix
1297 gel (Shandon Cryomatrix, Thermo Fisher Scientific, Waltham MA, USA) and sectioned coronally.
1298 Slices were 50 µm thick, transferred onto microscope slides (Thermo Superfrost/ColorFrost Plus,
1299 Charged 90° - CS/1440CS/1440, Erie Scientific, Ramsey MI, USA) and prepared for antibody
1300 staining. The staining follows the cochleae staining protocol, after PBS washing, sections were
1301 blocked with goat serum dilution buffer (GSDB) for 1h at room temperature before primary
1302 antibodies for parvalbumin (1:300, guinea pig, Synaptic Systems, Goettingen, Germany) and GFP
1303 (to label ChReef, 1:500, chicken, Abcam, Cambridge, UK). Goat anti-guinea-pig-568 and goat anti-
1304 chicken-488 were used for secondary antibodies and incubated at room temperature for 1h –
1305 slides were ultimately mounted with Mowiol and imaged the following day. Images were taken
1306 in oil at 40x using LSM510 (Zeiss, 467 Jena, Germany) microscope and analyzed with ImageJ (U.
1307 S. National Institutes of Health, Bethesda, Maryland, USA).

1308 **Immunostaining, confocal imaging and image analysis for cochlear cryosections of mice and**
1309 **Mongolian gerbils**

1310 Directly after the end of the optogenetic measurements, cochleae from both sides were prepared
1311 as previously described[14,18,40]. In short, samples were fixed for an hour in 4% paraformaldehyde
1312 (PFA), decalcified for 3-4 days in 0.12 M ethylenediaminetetraacetic acid (EDTA), dehydrated in
1313 25% sucrose solution for 24 hours and cryosectioned (mid-modiolar cryosections, 25 µm tick).
1314 Immunofluorescence staining were done in 16% goat serum dilution buffer (16% normal goat
1315 serum, 450 mM NaCl, 0.6% Triton X-100, 20 mM phosphate buffer, pH 7.4). The following primary
1316 antibodies were used at 4 °C overnight: chicken anti-GFP (1:500, ab13970 Abcam, USA) and
1317 guinea pig anti-parvalbumin (1:300, 195004 Synaptic Systems, Germany); and secondary
1318 antibodies for one hour in room temperature: goat anti-chicken 488 IgG (1:200, A-11039 Thermo
1319 Fisher Scientific, USA) and goat anti-guinea pig 568 IgG (1:200, A-1107 Thermo Fisher Scientific,
1320 USA). Finally, slices were mounted in Mowiol 4-88 (Carl Roth, Germany). Samples were imaged
1321 with a confocal microscope SP8 (Leica, Germany) mounted with a 40x oil objective. For each
1322 cochlear turn (apex, middle and base) an image was taken focusing on the modiolus.

1323 Image analysis was performed by a custom-written MATLAB script modified from[51]. Briefly, SGN
1324 somas and modiolus area were manually detected using a touch screen from the parvalbumin
1325 images. Next, individual somas were automatically segmented using Otsu's threshold method
1326 from every Z-stack and a mask corresponding to the given SGN was defined for the Z-stack for
1327 which the mask was fulfilling the criteria of size (area and diameter) and circularity. In case the
1328 segmentation was not correct, the segmentation of the given SGN soma was performed
1329 manually. Next, the median GFP brightness of each SGNs was measured and its distribution was

1330 fitted with a Gaussian mixture model with up to 3 components. A threshold, above which SGNs
1331 somas were considered as transduced, was defined as average + 3 x standard deviation of the
1332 Gaussian distribution with the lowest mean.

1333 To assess the subcellular expression profiles of ChRmine and ChReef in SGNs, we utilized a
1334 custom-written Python program to plot fluorescence line profiles, incorporating a manual
1335 verification process. The process began by using the manually detected centroids (as explained
1336 in the previous analysis) of all cells to generate 2D square crops of the images, each containing
1337 one complete SGN. For each 2D crop, the Z-plane was selected by maximizing fluorescence in the
1338 cytoplasmic parvalbumin channel.

1339 Cell membrane masks were automatically generated based on the cytoplasmic parvalbumin
1340 channel fluorescence using a fixed threshold. Line profiles were then automatically positioned
1341 perpendicular to these masks and avoiding intersection with surrounding cells. Manual
1342 verification of SGN masks and line profile positions was conducted using a custom graphical
1343 interface developed with Napari. The Z-plane was manually checked for a noticeable
1344 fluorescence drop indicating the nucleus's position; cells lacking a discernible nucleus were
1345 excluded to prevent bias from including line profiles in the nuclear region or parallel to the cell
1346 surface. Any line profiles that intersected visually identifiable nuclei were excluded from further
1347 analysis.

1348 Only cells and line profiles that passed manual verification were used in further analysis. Cells
1349 with fewer than three confirmed line profiles were automatically excluded. Fluorescence data
1350 from the YFP channel was recorded along each line profile and averaged across all lines for each

1351 cell, creating an expression line profile for each cell. These expression line profiles from all
1352 verified cells were then averaged, and the standard deviation was calculated.

1353

1354 **Methods of optogenetic stimulation of the auditory pathway in the common marmoset**

1355 **Animal housing**

1356 Data were obtained from nine 2.5 to 3.75 year old common marmosets of either sex (5 male, 4
1357 female). Animals were pair housed in a colony of about 50 animals consisting of several rooms
1358 with acoustic but no visual contact to neighboring pairs. The colony maintained a 12h:12h light-
1359 dark cycle at a temperature of 26 ± 1.5 °C and a relative humidity of 60 - 80 %. Animals were fed
1360 *ad libitum* a diet of fresh fruits, vegetables, nuts, arabic gum, rice, pasta, potatoes, meal worms,
1361 crickets, joghurt, various minerals as well as pellets. Water was always available and was
1362 occasionally mixed up with unsweetened tea.

1363 **Injection method**

1364 First, animals received Metacam (0.2 mg/kg BW) either orally – or if not possible – via s.c.
1365 injection and were anesthetized with injections of Alfaxan (10mg/kg BW, i.m.) and Midazolam
1366 (0.125 mg per animal, i.m.). Additionally, dexamethasone (5 mg/kg BW, i.m.) and Cerenia (1
1367 mg/kg BW, s.c.) were also applied. The fur around the surgical site was removed. Then, an
1368 intravenous catheter was placed in the vena saphena and the animal was intubated using a 00
1369 Miller blade and a custom-made unblocked endotracheal tube for artificial ventilation. Next,
1370 anesthesia was transferred to a combined volatile-intravenous anesthesia with Sevoflurane (ca.

1371 2 – 3 %) and Propofol-Remifentanil (0.3 – 0.4 mg/kg/min; 10 – 25 µg/kg/h, respectively) to effect.
1372 During surgery body temperature was maintained between 37 and 38°C with a heating pad and
1373 a forced air warming blanket wrapped around the animals' body. Additionally, physiological
1374 parameters were monitored throughout the surgery via ECG and pulse oximetry. Surgery itself
1375 was performed under standard aseptic technique. Local analgesia was achieved with Carbostesin
1376 injections around the surgical site. The cochlea was accessed via a retroauricular incision, blunt
1377 dissection of post-auricular as well as temporal muscles to expose the linea temporalis and
1378 mastoidectomy ventral to the linea temporalis. Utmost care was used to avoid damaging the
1379 horizontal semicircular canal and facial nerve which served as guiding landmarks. Animals were
1380 initially deafened with flushes of 10 % Neomycin as described previously [64]. In later experiments,
1381 Neomycin was added to the viral suspension to a final concentration of 10 %. In addition, the
1382 ossicle chain was disrupted by removal of the malleus. The viral suspension was administered
1383 either via a pipette pulled from borosilicate and pressure injection or a silicone catheter was used
1384 to slowly (15 µl/30 min; UMP3, World Precision Instruments) inject. In both cases, the round
1385 window membrane was identified and gently ruptured. To prevent pressure build-up inside the
1386 cochlea during slow injection, a ventilation hole was opened either with a rose burr next to the
1387 oval window or by removing the stapes when surgical access was favorable. Excess viral
1388 suspension was carefully suctioned to avoid unwanted transfection of surrounding tissue. In later
1389 experiments, Dexamethasone was added to the viral suspension (2 %). Three different titers of
1390 viral suspension (15µl) were used 5x 10^{10} , 10^{11}, und 5x 10^{11} GC) and injected in three animals
1391 each. Animals were randomly assigned to each group and experimenters were blinded to the
1392 condition. After virus injection the round window and vent holes were closed with autologous

1393 tissue, the mastoidectomy closed by replacing the temporal and post-auricular muscles. The skin
1394 and muscles were then sutured with 5/0 absorbable suture. For direct post-operative pain
1395 management, Buprenorphine (0.005 mg/kg BW, s.c.) was administered. To prevent hypoglycemia
1396 Glucose (5%, 2 ml) was administered s.c. Post-operative care included repeated antibiotic
1397 administration (Amoxicillin 37.5 mg/kg BW) every 48 h for 8 days as well as analgesia via
1398 Metacam administration (0.2 mkg/kg BW, p.o.).

1399 **Acoustic auditory brainstem recordings**

1400 Hearing status of animals was assessed with a custom built mobile audiometry setup twice
1401 throughout the experiment: first several weeks before virus injection and second after a recovery
1402 period of 2 to 4 weeks after virus injection. Towards this, animals were anesthetized with a
1403 mixture of Alfaxan (10mg/kg BW, i.m.) and Midazolam (0.125 mg per animal, i.m.). Further,
1404 Metacam (0.2 mg/kg BW) was administered either orally – or if not possible – via s.c. injection.
1405 After anesthesia initiation animals were placed on a heat pad, wrapped in a forced air warming
1406 blanket and body temperature maintained at 37 to 38 °C. Otoscopic evaluation of ear canals was
1407 performed next to rule out signs of infection and was found to be normal in all cases. Afterwards,
1408 animals were transferred onto a warmed saline bag on a heat pad within a stereotaxic frame.
1409 Animals were not fixed inside the frame but made use of custom-made ear bars containing
1410 earphone (Etymotic ER-4PT) and microphone (Sennheiser MKE 2 P-C) inserts. Ear bars were
1411 gently inserted into the outer ear canals. Monitoring of the microphone signal upon acoustic
1412 stimulation ensured correct placement. Auditory stimuli were calibrated separately with 3D
1413 printed ear molds of common marmosets where a 1/8th inch microphone (G.R.A.S. 46 BE) was
1414 placed at the position of the tympanic membrane. Stimulus generation and delivery, as well as

1415 data acquisition was performed using a custom-written software (MATLAB, MathWorks, Natick,
1416 MA, United States) employing National Instrument data acquisition cards and a custom-build
1417 laser-controller. Recordings were conducted in a dedicated operating theater for non-human
1418 primate surgery. If necessary, anesthesia was maintained by re-injecting Alfaxan (5 mg/kg BW).
1419 Acoustically evoked ABRs (aABRs) were recorded by placing needle electrodes behind the pinna,
1420 on the vertex, and on the neck of the anesthetized animals. The difference in potential between
1421 the vertex and mastoid subdermal needles was amplified using a custom-designed amplifier,
1422 sampled at a rate of 50 kHz for 10 ms, filtered (300–3000 Hz) and averaged across at least 750
1423 stimulus presentations. In case of pure tone stimulation a bandpass filter centered on the pure
1424 tone frequency removed stimulus artifacts observed sometimes. The ABRs threshold was defined
1425 and determined as the lowest light or sound intensity for which one of the 5 waves (aABR) or 2
1426 waves (oABR) was reliably visible.

1427 **Optically driven auditory brainstem recordings**

1428 11 (± 3 SD) weeks after virus injection, animals were subjected to *in vivo* optical stimulation and
1429 recordings. Here, the general surgical and anesthesia procedure was the same as for the virus
1430 application. After again a retroauricular incision, to avoid excessive bleeding due to scar tissue
1431 development, the surgical approach to the cochlea was adjusted and included removal of the
1432 posterior bony part of the ear canal. Next, needle electrodes were placed behind the pinna, on
1433 the vertex, and on the neck and the difference in potential between the vertex and mastoid
1434 subdermal needles was amplified and treated as described for the aABR measurements above.
1435 A 200 µm optical fiber coupled to both a 525 nm (Oxxius, France) and a 488 nm (OBIS) laser was
1436 used for optical stimulation. Laser power was calibrated prior to each experiment using a laser

1437 power meter (Gentec EO-Solo , or S140C Thorlabs, Germany). After the cessation of optical
1438 stimulation experiments, animals were euthanized under deep anesthesia via an injection of an
1439 overdose of pentobarbital and transcardially perfused with 4 % FA with the descending aorta
1440 clamped.

1441 **Immunostaining and confocal imaging of cochlear cryosections**

1442 After euthanasia, temporal bones were postfixated in 4 % FA for 48 h. The facial nerves exiting
1443 the foramen stylomastoideus were dissected and the soft tissue overlying the temporal bones
1444 were removed to allow trimming bone around the cochlea under visual guidance. Next, the
1445 cochlea and vestibular organs were transferred into 5 M EDTA for decalcification. During a period
1446 of at least 2 weeks, EDTA was regularly exchanged and softened bone removed from the cochlea.
1447 Additionally, the facial nerve was removed from its bony capsule overlying the cochlea. Once
1448 completed, the cochlea was prepared for whole mounts of the organ of Corti and mid-modiolar
1449 cochlear cryosections. Here, the spiral ligament and bone lamella of the apex were carefully
1450 removed to access the organ of Corti and dissecting it by cutting the spiral lamina. Next, the stria
1451 vascularis and tectorial membrane were removed. This procedure was repeated until the whole
1452 organ of Corti was dissected into consecutive whole mounts and the cochlear modiolus. Finally,
1453 the whole mounts and modioli were stored in phosphate buffered saline. The modioli were then
1454 processed similarly to rodent samples: after a 24 h dehydration step in 25 % sucrose solution,
1455 samples were cryosectioned (mid-modiolar cryosections, 16 µm tick). Immunofluorescence
1456 staining was performed in 16% goat serum dilution buffer (16% normal goat serum, 450 mM
1457 NaCl, 0.6% Triton X-100, 20 mM phosphate buffer, pH 7.4). The following primary antibodies
1458 were used at 4 °C overnight: chicken anti-GFP (1:500, ab13970 Abcam, USA) and guinea pig anti-

1459 parvalbumin (1:300, 195004 Synaptic Systems, Germany) as well as mouse anti-NF200 (1:400,
1460 Sigma, St. Louis, USA); and secondary antibodies for one hour in room temperature: goat anti-
1461 chicken 488 IgG (1:200, Invitrogen Scientific, USA), goat anti-guinea pig 568 IgG (1:200,
1462 Invitrogen, USA) and anti-mouse 633 (1:200, Invitrogen). Finally, slices were mounted in Mowiol
1463 4-88 (Carl Roth, Germany). Whole mounts were first permeabilized with TritonX 0,5% in PBS.
1464 Staining was then performed in 10 % goat serum dilution buffer and guinea pig anti-parvalbumin
1465 (1:200; Synaptic systems, Germany), rabbit anti-Otoferlin (1:500; SySy) and chicken anti-GFP
1466 (1:500; Abcam) were used as primary antibodies. As secondary antibodies anti-chicken 488
1467 (1:1000; Invitrogen), anti-guinea pig 568 (1:1000; Invitrogen) and anti-rabbit 633 (1:1000;
1468 Thermo Fisher) were used. Samples were imaged with a confocal microscope SP8 (Leica,
1469 Germany) mounted with a 40x oil objective. For each cochlear turn (apex, middle and base) an
1470 image was taken focusing on the modiolus. Image analysis was performed by a custom-written
1471 MATLAB script modified from[65]. Briefly, SGN somas and modiolus area were manually detected
1472 using a touch screen from the parvalbumin images. Next, individual somas were automatically
1473 segmented using Otsu's threshold method from every Z-stack and a mask corresponding to the
1474 given SGN was defined for the Z-stack for which the mask was fulfilling the criteria of size (area
1475 and diameter) and circularity. In case the segmentation was not right, the segmentation of the
1476 given SGN soma was performed manually. Next, the median GFP brightness of each SGNs was
1477 measured and its distribution was fitted with a Gaussian mixture model with up to 3 components.
1478 A threshold, above which SGNs somas were considered as transduced, was defined as average +
1479 3 x standard deviation of the Gaussian distribution with the lowest mean. The density of inner

1480 hair cells (IHCs) along the whole mounts was calculated by placing a curve along the (presumed)
1481 IHC, measuring its length and assessing the number of identified IHC.

1482 **Data analysis**

1483 During the injection, oABR measurements as well as histological analysis, experimenters were
1484 blinded to the experimental group. Unblinding was performed afterwards.

1485

1486 **Data availability statement:** The data that support the findings of this study is available from the
1487 corresponding authors upon reasonable request.

1488 **Code availability statement:** The code used for analysis is available from the corresponding
1489 authors upon reasonable request.

1490

1491 **Acknowledgements**

1492 We thank Christiane Senger-Freitag for expert help with cloning of the ChR constructs and
1493 excellent technical support. The authors gratefully acknowledge Daniela Gerke for virus
1494 production and histology of auditory samples. We thank Tamara Becker for expert veterinary
1495 work on marmosets. We further gratefully acknowledge Anupriya Thirumalai for assistance
1496 image analysis. We thank Gerhard Hoch for excellent technical support, and Patricia Räke-Kügler
1497 for excellent administrative support. We thank Julia Kuhl for her help on figure illustrations. We
1498 thank Aude Villemain for maintaining mouse colonies and assisting with intravitreal injections.
1499 We thank Shijie Tong for assistance with the Bonsai pipeline for tracking mice in the light-room.
1500 The European Research Council through the Advanced Grant 'OptoHear" to TM under the
1501 European Union's Horizon 2020 Research and Innovation program (grant agreement No. 670759)
1502 as well as in the project OptoWave (ERC Proof-of-Concept grant, Horizon 2022) and the
1503 Fraunhofer and Max-Planck cooperation program (NeurOpto grant) supported by pact for

research and innovation. Further support came from German Research Foundation through the Cluster of Excellence (EXC2067) Multiscale Bioimaging (TM, TMa, TB, EM) and the Leibniz Program to TM. Furthermore, this work was also supported by the Ernst Jung Prize for Medicine and by Fondation Pour l'Audition (FPA RD-2020-10) and received funding by Volkswagen-Stiftung from the "Niedersächsisches Vorab" (ZN3898 and ZN4000) (to TM). AG was supported by Alexander von Humboldt Foundation. VH and FE are fellows of the German Academic Scholarship Foundation (Studienstiftung des Deutschen Volkes). TB was supported and funded by the German Centre for Cardiovascular Research (DZHK), the Deutsche Forschungsgesellschaft (DFG, German Research Foundation: Germany's Excellence Strategy (EXC 2067/1-390729940), IRTG1826 (200857327, Svenja Kiehn); Priority Program 1926 (315212873), CRC1002 (193793266, project A14), clinician scientist program 413501650 to MH and project 452139556. D.S. was supported by the Swiss National Science Foundation (SNSF) Early Postdoc Mobility no. 194957, SNSF Postdoc. Mobility no. 211087 and Deutsche Forschungsgemeinschaft Walter-Benjamin Programm (Stelle) no. SI 2831/1-1. KRDG was supported by FRQS (301004) and CONACYT (773971) PhD fellowships and ST by a Canada Research Chair, a Canadian Institutes of Health Research Project Grant (398769), and an Early-Career Capacity Building Grant from Brain Canada and the Azrieli Foundation.

Author contributions

TM, TMa, BW, EM and TB designed the research. ChR construct design and mutagenesis were conducted by TMa. In vitro characterization was a collaborative effort by MZ, AA, AG and IW under supervision of TMa. Virus design and production was done by KK. Optogenetic cardiac stimulation experiments were performed by MH, SMK, MA, LC, and TB. Optogenetic vision restoration research was undertaken by DS, KDRG, ST, and EM. VH, TA, FE, AV, and BW performed the optogenetic stimulation of the auditory periphery with supervision of TM. Marmoset work was performed by MJ, AM, BW, AH, KK and AR. MZ, TH, AA, AV, FE, DS, TB and TA prepared figures with input from other authors. TM, TMa, and BW wrote the paper with contributions of

EM, TB. TM, EM and TB acquired funding. All authors have reviewed and approved the final version of the manuscript for submission.

Competing interests

TM is co-founder of the OptoGenTech Company. TM, MZ and TMa are authors on a pending patent application related to this work, filed by Universitaetsmedizin Goettingen and OptoGenTech (EPA-22155173). Remaining authors declare no conflict of interest.

References

1. Emiliani, V. *et al.* Optogenetics for light control of biological systems. *Nat. Rev. Methods Primer* **2**, 1–25 (2022).
2. Sahel, J.-A. *et al.* Partial recovery of visual function in a blind patient after optogenetic therapy. *Nat. Med.* **27**, 1223–1229 (2021).
3. Feldbauer, K. *et al.* Channelrhodopsin-2 is a leaky proton pump. *Proc. Natl. Acad. Sci.* **106**, 12317–12322 (2009).
4. Kleinlogel, S., Vogl, C., Jeschke, M., Neef, J. & Moser, T. Emerging Approaches for Restoration of Hearing and Vision. *Physiol. Rev.* **100**, 1467–1525 (2020).
5. Dieter, A., Keppeler, D. & Moser, T. Towards the optical cochlear implant: optogenetic approaches for hearing restoration. *EMBO Mol. Med.* **12**, e11618 (2020).
6. Govorunova, E. G., Sineshchekov, O. A., Janz, R., Liu, X. & Spudich, J. L. Natural light-gated anion channels: A family of microbial rhodopsins for advanced optogenetics. *Science* **349**, 647–650 (2015).
7. Govorunova, E. G. *et al.* Kalium channelrhodopsins are natural light-gated potassium channels that mediate optogenetic inhibition. *Nat. Neurosci.* **25**, 967–974 (2022).

1554 8. Marshel, J. H. *et al.* Cortical layer–specific critical dynamics triggering perception. *Science* **365**,
1555 eaaw5202 (2019).
1556 9. Kishi, K. E. *et al.* Structural basis for channel conduction in the pump-like channelrhodopsin
1557 ChRmine. *Cell* **185**, 672-689.e23 (2022).
1558 10. Sineshchekov, O. A. *et al.* Conductance Mechanisms of Rapidly Desensitizing Cation
1559 Channelrhodopsins from Cryptophyte Algae. *mBio* **11**, 10.1128/mbio.00657-20 (2020).
1560 11. Hsueh, B. *et al.* Cardiogenic control of affective behavioural state. *Nature* **615**, 292–299 (2023).
1561 12. Chen, R. *et al.* Deep brain optogenetics without intracranial surgery. *Nat. Biotechnol.* **39**, 161–164
1562 (2021).
1563 13. Gradinaru, V. *et al.* Molecular and Cellular Approaches for Diversifying and Extending Optogenetics.
1564 *Cell* **141**, 154–165 (2010).
1565 14. Keppeler, D. *et al.* Ultrafast optogenetic stimulation of the auditory pathway by targeting-optimized
1566 Chronos. *EMBO J.* **37**, e99649 (2018).
1567 15. Yoshino, M. & Murakami, K. Analysis of the substrate inhibition of complete and partial types.
1568 *SpringerPlus* **4**, 292 (2015).
1569 16. *Single-Channel Recording*. (Springer, New York, NY, 2009).
1570 17. Kleinlogel, S. *et al.* Ultra light-sensitive and fast neuronal activation with the Ca^{2}+-permeable
1571 channelrhodopsin CatCh. *Nat. Neurosci.* **14**, 513–518 (2011).
1572 18. Mager, T. *et al.* High frequency neural spiking and auditory signaling by ultrafast red-shifted
1573 optogenetics. *Nat. Commun.* **9**, 1750 (2018).
1574 19. Saita, M. *et al.* Photoexcitation of the P4480 State Induces a Secondary Photocycle That Potentially
1575 Desensitizes Channelrhodopsin-2. *J. Am. Chem. Soc.* **140**, 9899–9903 (2018).
1576 20. Kuhne, J. *et al.* Unifying photocycle model for light adaptation and temporal evolution of cation
1577 conductance in channelrhodopsin-2. *Proc. Natl. Acad. Sci.* **116**, 9380–9389 (2019).

1578 21. Ganjawala, T. H., Lu, Q., Fenner, M. D., Abrams, G. W. & Pan, Z.-H. Improved CoChR Variants Restore
1579 Visual Acuity and Contrast Sensitivity in a Mouse Model of Blindness under Ambient Light
1580 Conditions. *Mol. Ther. J. Am. Soc. Gene Ther.* **27**, 1195–1205 (2019).
1581 22. Bruegmann, T. *et al.* Optogenetic defibrillation terminates ventricular arrhythmia in mouse hearts
1582 and human simulations. *J. Clin. Invest.* **126**, 3894–3904 (2016).
1583 23. Nyns, E. C. A. *et al.* Optogenetic termination of ventricular arrhythmias in the whole heart: towards
1584 biological cardiac rhythm management. *Eur. Heart J.* **38**, 2132–2136 (2017).
1585 24. Crocini, C. *et al.* Optogenetics design of mechanistically-based stimulation patterns for cardiac
1586 defibrillation. *Sci. Rep.* **6**, 35628 (2016).
1587 25. Bruegmann, T., Beiert, T., Vogt, C. C., Schrickel, J. W. & Sasse, P. Optogenetic termination of atrial
1588 fibrillation in mice. *Cardiovasc. Res.* **114**, 713–723 (2018).
1589 26. Nyns, E. C. A. *et al.* An automated hybrid bioelectronic system for autogenous restoration of sinus
1590 rhythm in atrial fibrillation. *Sci. Transl. Med.* **11**, (2019).
1591 27. Richter, C. & Bruegmann, T. No light without the dark: Perspectives and hindrances for translation
1592 of cardiac optogenetics. *Prog. Biophys. Mol. Biol.* **154**, 39–50 (2020).
1593 28. Sasse, P., Funken, M., Beiert, T. & Bruegmann, T. Optogenetic Termination of Cardiac Arrhythmia:
1594 Mechanistic Enlightenment and Therapeutic Application? *Front. Physiol.* **10**, 675 (2019).
1595 29. Pyari, G., Bansal, H. & Roy, S. Ultra-low power deep sustained optogenetic excitation of human
1596 ventricular cardiomyocytes with red-shifted opsins: a computational study. *J. Physiol.* **600**, 4653–
1597 4676 (2022).
1598 30. Chang, B. *et al.* Retinal degeneration mutants in the mouse. *Vis. Res* **42**, 517–525 (2002).
1599 31. Norton, T. T. & Siegwart, J. T. Light levels, refractive development, and myopia--a speculative
1600 review. *Exp. Eye Res.* **114**, 48–57 (2013).

1601 32. Berry, M. H. *et al.* Restoration of patterned vision with an engineered photoactivatable G protein-
1602 coupled receptor. *Nat. Commun.* **8**, 1862 (2017).
1603 33. Bourin, M. & Hascoët, M. The mouse light/dark box test. *Eur. J. Pharmacol.* **463**, 55–65 (2003).
1604 34. Wolf, B. J. *et al.* Is there an unmet medical need for improved hearing restoration? *EMBO Mol. Med.*
1605 **14**, e15798 (2022).
1606 35. Dieter, A., Duque-Afonso, C. J., Rankovic, V., Jeschke, M. & Moser, T. Near physiological spectral
1607 selectivity of cochlear optogenetics. *Nat. Commun.* **10**, 1962 (2019).
1608 36. Dieter, A. *et al.* µLED-based optical cochlear implants for spectrally selective activation of the
1609 auditory nerve. *EMBO Mol. Med.* e12387 (2020) doi:10.15252/emmm.202012387.
1610 37. Saeedi, A., Englert, L. & Hemmert, W. eABR THR Estimation Using High-Rate Multi-Pulse Stimulation
1611 in Cochlear Implant Users. *Front. Neurosci.* **15**, 705189 (2021).
1612 38. Roux, I. *et al.* Otoferlin, Defective in a Human Deafness Form, Is Essential for Exocytosis at the
1613 Auditory Ribbon Synapse. *Cell* **127**, 277–289 (2006).
1614 39. Taberner, A. M. & Liberman, M. C. Response Properties of Single Auditory Nerve Fibers in the
1615 Mouse. *J. Neurophysiol.* **93**, 557–569 (2005).
1616 40. Bali, B. *et al.* Utility of red-light ultrafast optogenetic stimulation of the auditory pathway. *EMBO*
1617 *Mol. Med.* **13**, e13391 (2021).
1618 41. Wrobel, C. *et al.* Optogenetic stimulation of cochlear neurons activates the auditory pathway and
1619 restores auditory-driven behavior in deaf adult gerbils. *Sci. Transl. Med.* **10**, eaao0540 (2018).
1620 42. Mittring, A., Moser, T. & Huet, A. T. Graded optogenetic activation of the auditory pathway for
1621 hearing restoration. *Brain Stimulat.* **16**, 466–483 (2023).
1622 43. Keppeler, D. *et al.* Multichannel optogenetic stimulation of the auditory pathway using
1623 microfabricated LED cochlear implants in rodents. *Sci. Transl. Med.* **12**, eabb8086 (2020).

1624 44. Friesen, L. M., Shannon, R. V. & Cruz, R. J. Effects of stimulation rate on speech recognition with
1625 cochlear implants. *Audiol. Neurootol.* **10**, 169–184 (2005).
1626 45. Marshel, J. H. *et al.* Cortical layer–specific critical dynamics triggering perception. *Science* **365**,
1627 eaaw5202 (2019).
1628 46. Klapoetke, N. C. *et al.* Independent optical excitation of distinct neural populations. *Nat. Methods*
1629 **11**, 338–346 (2014).
1630 47. Nagel, G. *et al.* Channelrhodopsin-2, a directly light-gated cation-selective membrane channel. *Proc.*
1631 *Natl. Acad. Sci. U. S. A.* **100**, 13940–13945 (2003).
1632 48. Yamauchi, Y. *et al.* Molecular properties of a DTD channelrhodopsin from *Guillardia theta*. *Biophys.*
1633 *Physicobiology* **14**, 57–66 (2017).
1634 49. Sineshchekov, O. A., Govorunova, E. G., Li, H. & Spudich, J. L. Bacteriorhodopsin-like
1635 channelrhodopsins: Alternative mechanism for control of cation conductance. *Proc. Natl. Acad. Sci.*
1636 *U. S. A.* **114**, E9512–E9519 (2017).
1637 50. Tabebordbar, M. *et al.* Directed evolution of a family of AAV capsid variants enabling potent muscle-
1638 directed gene delivery across species. *Cell* **184**, 4919-4938.e22 (2021).
1639 51. Huet, A. T. & Rankovic, V. Application of Targeting-Optimized Chronos for Stimulation of the
1640 Auditory Pathway. in *Methods in Molecular Biology (Clifton, N.J.)* vol. 2191 261–285 (2021).
1641 52. Challis, R. C. *et al.* Systemic AAV vectors for widespread and targeted gene delivery in rodents. *Nat.*
1642 *Protoc.* **14**, 379–414 (2019).
1643 53. Cyganek, L. *et al.* Deep phenotyping of human induced pluripotent stem cell–derived atrial and
1644 ventricular cardiomyocytes. *JCI Insight* **3**, (2018).
1645 54. Kleinsorge, M. & Cyganek, L. Subtype-Directed Differentiation of Human iPSCs into Atrial and
1646 Ventricular Cardiomyocytes. *STAR Protoc.* **1**, 100026 (2020).

1647 55. Peirce, J. *et al.* PsychoPy2: Experiments in behavior made easy. *Behav. Res. Methods* **51**, 195–203
1648 (2019).
1649 56. Pachitariu, M., Sridhar, S. & Stringer, C. Solving the spike sorting problem with Kilosort.
1650 2023.01.07.523036 Preprint at https://doi.org/10.1101/2023.01.07.523036 (2023).
1651 57. Morel, P. Gramm: grammar of graphics plotting in Matlab. *J. Open Source Softw.* **3**, 568 (2018).
1652 58. Maris, E. & Oostenveld, R. Nonparametric statistical testing of EEG- and MEG-data. *J. Neurosci.*
1653 *Methods* **164**, 177–190 (2007).
1654 59. Cazemier, J. L. *et al. Involvement of Superior Colliculus in Complex Figure Detection of Mice*.
1655 http://biorxiv.org/lookup/doi/10.1101/2022.09.25.509365 (2022) doi:10.1101/2022.09.25.509365.
1656 60. Lopes, G. *et al.* Bonsai: an event-based framework for processing and controlling data streams.
1657 *Front. Neuroinformatics* **9**, (2015).
1658 61. Reisinger, E. *et al.* Probing the functional equivalence of otoferlin and synaptotagmin 1 in
1659 exocytosis. *J. Neurosci.* **31**, 4886–4895 (2011).
1660 62. Butola, T. *et al.* RIM-Binding Protein 2 Organizes Ca2+ Channel Topography and Regulates Release
1661 Probability and Vesicle Replenishment at a Fast Central Synapse. *J. Neurosci.* **41**, 7742–7767 (2021).
1662 63. Schneider, C. A., Rasband, W. S. & Eliceiri, K. W. NIH Image to ImageJ: 25 years of image analysis.
1663 *Nat. Methods* **9**, 671–675 (2012).
1664 64. Johnson, L. A., Della Santina, C. C. & Wang, X. Selective Neuronal Activation by Cochlear Implant
1665 Stimulation in Auditory Cortex of Awake Primate. *J. Neurosci.* **36**, 12468–12484 (2016).
1666 65. Huet, A. T., Dombrowski, T., Rankovic, V., Thirumalai, A. & Moser, T. Developing Fast, Red-Light
1667 Optogenetic Stimulation of Spiral Ganglion Neurons for Future Optical Cochlear Implants. *Front.*
1668 *Mol. Neurosci.* **14**, 635897 (2021).
1669

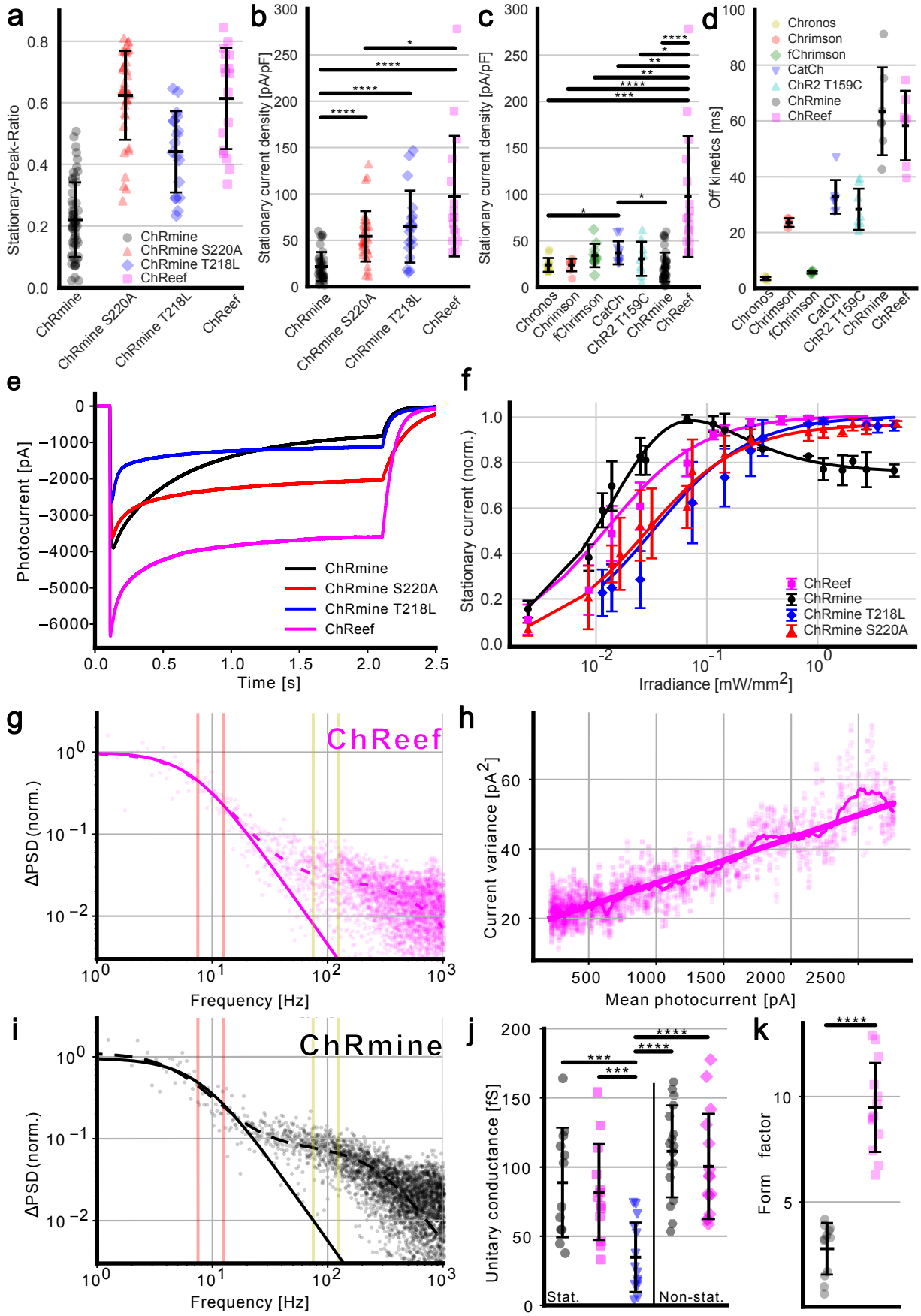
a
Stationary-Peak-Ratio
ChRmine
ChRmine S220A
ChRmine T218L
ChReef
b
Stationary current density [pA/pF]
c
Chronos
Chrimson
fChrimson
CatCh
ChR2 T159C
d
Off kinetics [ms]
e
Photocurrent [pA]
Time [s]
f
Stationary current (norm.)
Irradiance [mW/mm2]
g
ChReef
ΔPSD (norm.)
Frequency [Hz]
h
Current variance [pA2]
Mean photocurrent [pA]
i
ChRmine
j
Unitary conductance [fS]
Stat.
Non-stat.
k
Form factor

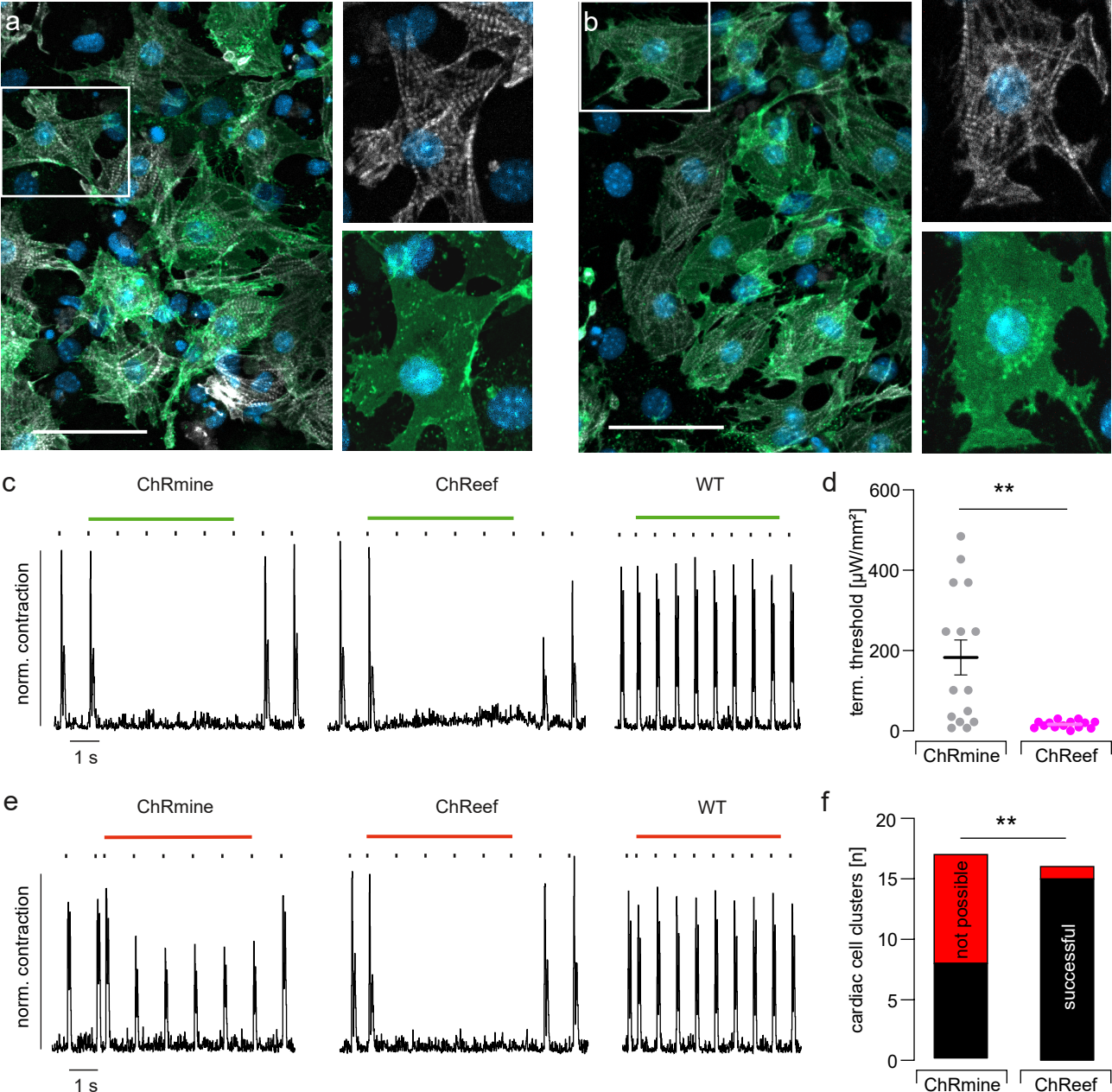
a
b
c
ChRmine
ChReef
WT
norm. contraction
1 s
d
**
term. threshold [µW/mm²]
600
400
200
0
ChRmine
ChReef
e
ChRmine
ChReef
WT
norm. contraction
1 s
f
**
cardiac cell clusters [n]
20
15
10
5
0
not possible
successful
ChRmine
ChReef

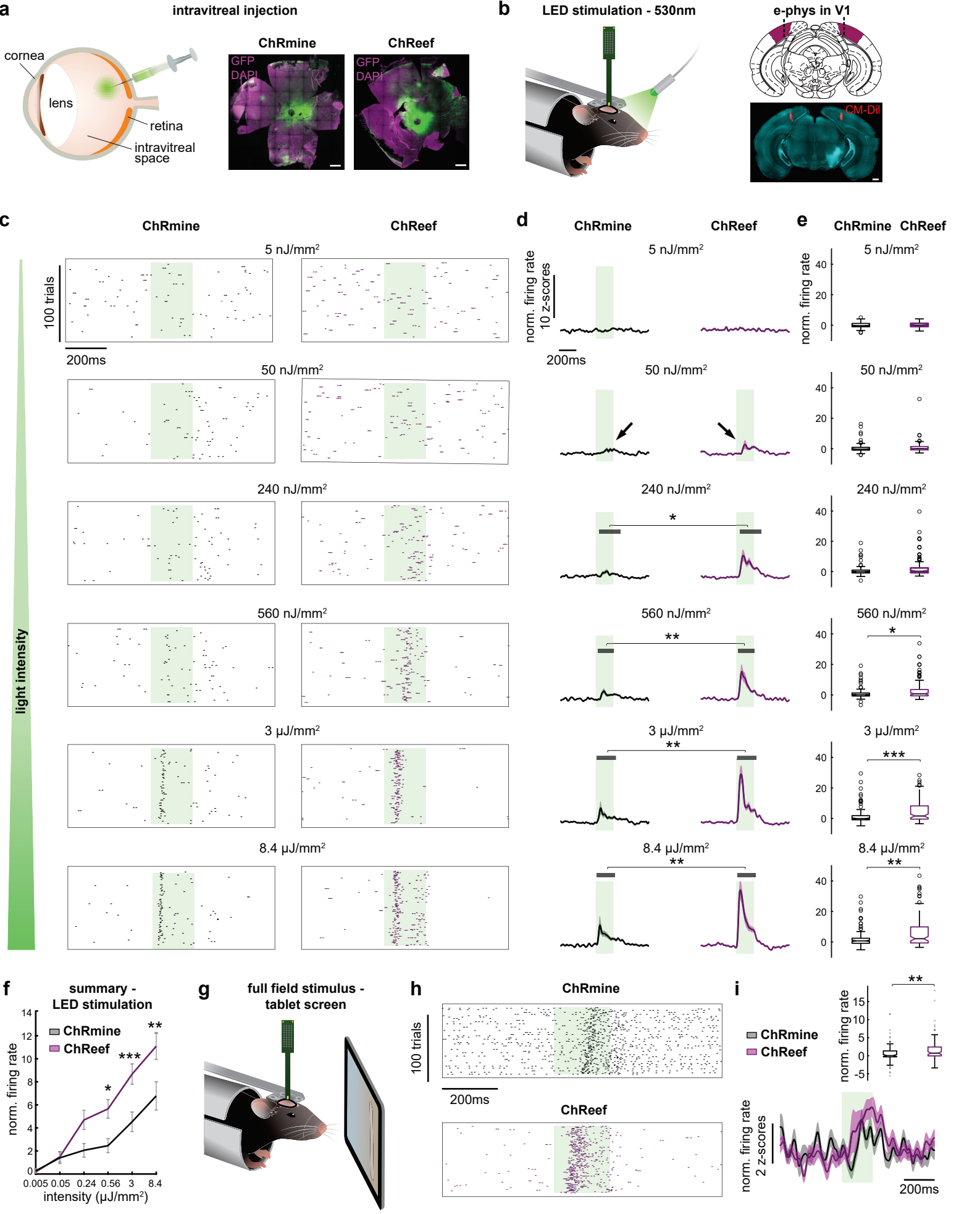
a
intravitreal injection
cornea
lens
retina
intravitreal space
ChRmine
ChReef
GFP
DAPI
b
LED stimulation - 530nm
e-phys in V1
CM-DiI
c
ChRmine
ChReef
5 nJ/mm²
50 nJ/mm²
240 nJ/mm²
560 nJ/mm²
3 μJ/mm²
8.4 μJ/mm²
100 trials
200ms
light intensity
d
norm. firing rate
10 z-scores
e
norm. firing rate
f
summary - LED stimulation
ChRmine
ChReef
norm. firing rate
intensity (μJ/mm²)
g
full field stimulus - tablet screen
h
ChRmine
ChReef
100 trials
200ms
i
ChRmine
ChReef
norm. firing rate
norm. firing rate
2 z-scores
200ms

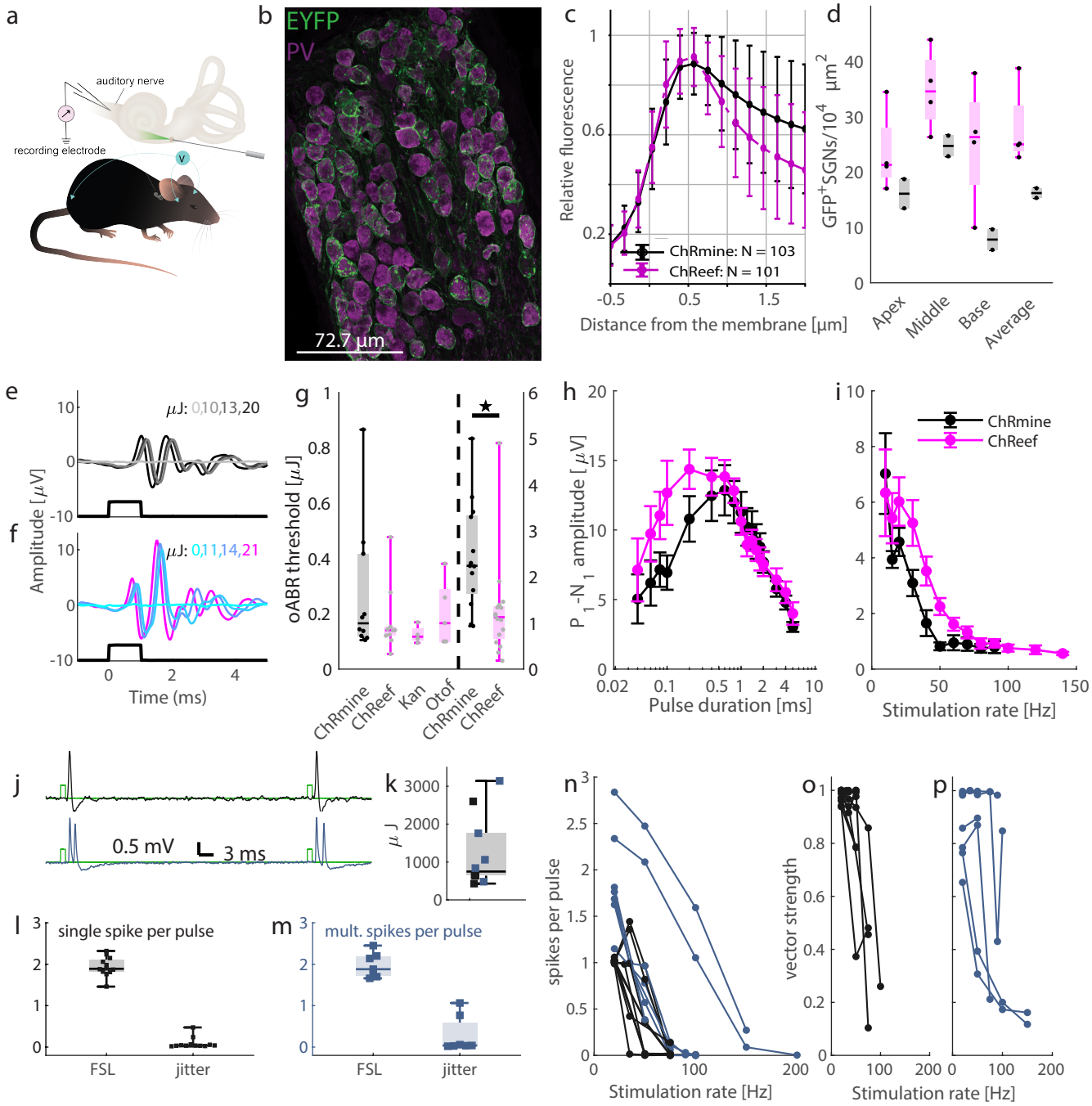
a
auditory nerve
recording electrode
b
EYFP
PV
72.7 µm
c
Relative fluorescence
ChRmine: N = 103
ChReef: N = 101
Distance from the membrane [µm]
d
GFP+SGNs/10^4 µm^2
Apex
Middle
Base
Average
e
µJ: 0,10,13,20
f
µJ: 0,11,14,21
Amplitude [µV]
Time (ms)
g
oABR threshold [µJ]
ChRmine
ChReef
Kan
Otof
ChRmine
ChReef
h
P1-N1 amplitude [µV]
Pulse duration [ms]
i
ChRmine
ChReef
Stimulation rate [Hz]
j
0.5 mV
3 ms
k
µJ
l
single spike per pulse
FSL
jitter
m
mult. spikes per pulse
FSL
jitter
n
spikes per pulse
Stimulation rate [Hz]
o
vector strength
Stimulation rate [Hz]
p

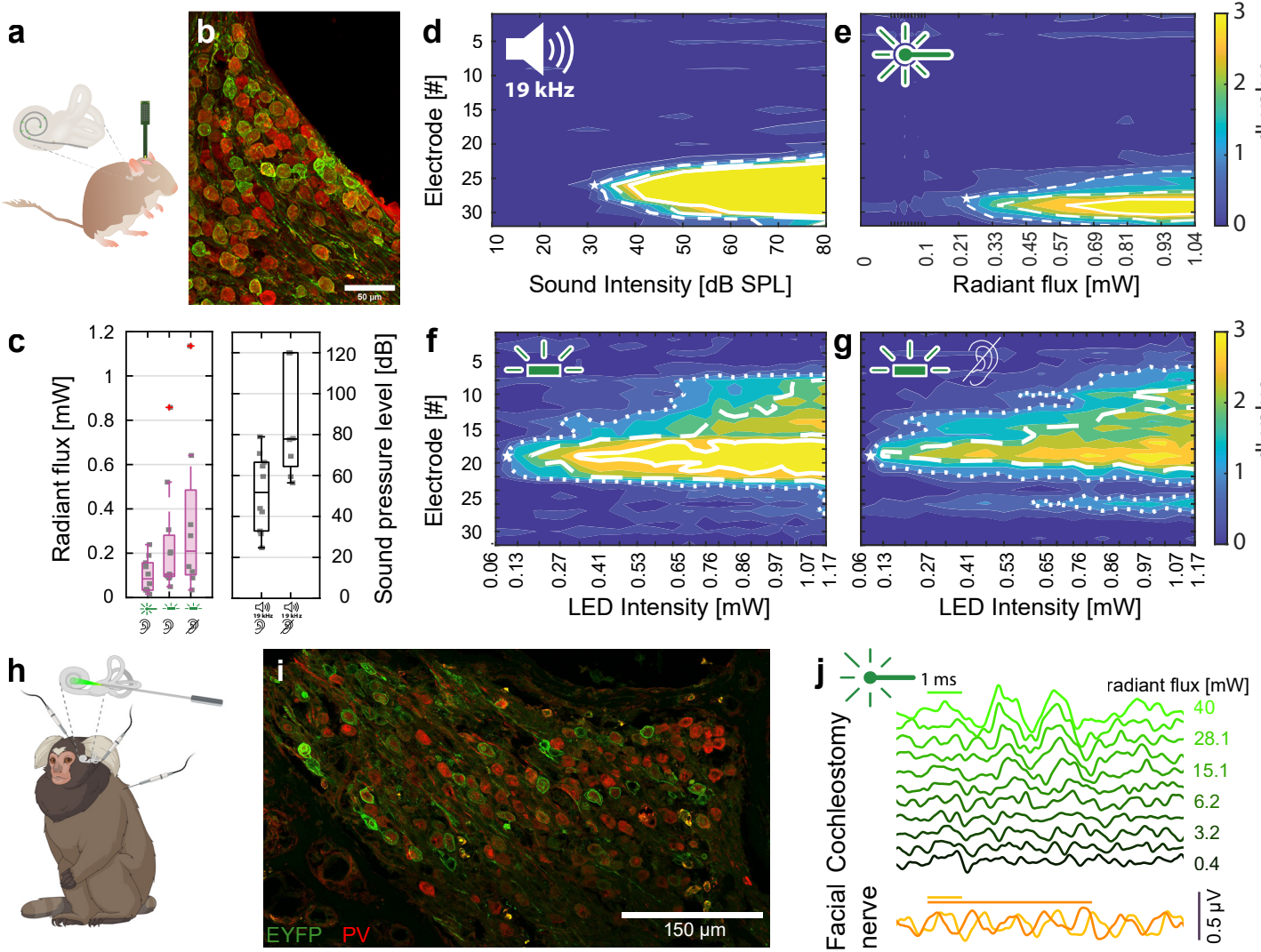
a
b
50 µm
c
Radiant flux [mW]
Sound pressure level [dB]
d
19 kHz
Electrode [#]
Sound Intensity [dB SPL]
e
Radiant flux [mW]
d'-value
f
g
LED Intensity [mW]
h
i
EYFP
PV
150 µm
j
1 ms
radiant flux [mW]
40
28.1
15.1
6.2
3.2
0.4
Cochleostomy
Facial nerve
0.5 µV